A&A 587, A55 (2016)
DOI: 10.1051/0004-6361/201526465

Astronomy & Astrophysics

First light of the VLT planet finder SPHERE

I. Detection and characterization of the substellar companion GJ 758 B⋆

A. Vigan[1,2], M. Bonnefoy[3,4], C. Ginski[5], H. Beust[3,4], R. Galicher[6], M. Janson[7,8], J.-L. Baudino[6], E. Buenzli[8], J. Hagelberg[9,10], V. D'Orazi[11,12,13], S. Desidera[11], A.-L. Maire[11], R. Gratton[11], J.-F. Sauvage[14,1], G. Chauvin[3,4], C. Thalmann[15], L. Malo[16], G. Salter[1], A. Zurlo[1,17,18], J. Antichi[19], A. Baruffolo[11], P. Baudoz[6], P. Blanchard[1], A. Boccaletti[6], J.-L. Beuzit[3,4], M. Carle[1], R. Claudi[11], A. Costille[1], A. Delboulbé[3,4], K. Dohlen[1], C. Dominik[20], M. Feldt[8], T. Fusco[14,1], L. Gluck[3,4], J. Girard[2,3,4], E. Giro[11], C. Gry[1], T. Henning[8], N. Hubin[21], E. Hugot[1], M. Jaquet[1], M. Kasper[21,3,4], A.-M. Lagrange[3,4], M. Langlois[22,1], D. Le Mignant[1], M. Llored[1], F. Madec[1], P. Martinez[23], D. Mawet[2,24], D. Mesa[11], J. Milli[2,3,4], D. Mouillet[3,4], T. Moulin[3,4], C. Moutou[1,16], A. Origné[1], A. Pavlov[8], D. Perret[6], C. Petit[14], J. Pragt[25], P. Puget[3,4], P. Rabou[3,4], S. Rochat[3,4], R. Roelfsema[25], B. Salasnich[11], H.-M. Schmid[15], A. Sevin[6], R. Siebenmorgen[21], A. Smette[2], E. Stadler[3,4], M. Suarez[21], M. Turatto[11], S. Udry[10], F. Vakili[23], Z. Wahhaj[2,1], L. Weber[10], and F. Wildi[10]

(Affiliations can be found after the references)

Received 4 May 2015 / Accepted 5 November 2015

ABSTRACT

GJ 758 B is a brown dwarf companion to a nearby (15.76%) solar-type, metal-rich (M/H = +0.2 dex) main-sequence star (G9V) that was discovered with Subaru/HiCIAO in 2009. From previous studies, it has drawn attention as being the coldest (~600 K) companion ever directly imaged around a neighboring star. We present new high-contrast data obtained during the commissioning of the SPHERE instrument at the Very Large Telescope (VLT). The data was obtained in Y-, J-, H-, and K_s-bands with the dual-band imaging (DBI) mode of IRDIS, thus providing a broad coverage of the full near-infrared (near-IR) range at higher contrast and better spectral sampling than previously reported. In this new set of high-quality data, we report the re-detection of the companion, as well as the first detection of a new candidate closer-in to the star. We use the new eight photometric points for an extended comparison of GJ 758 B with empirical objects and four families of atmospheric models. From comparison to empirical object, we estimate a T8 spectral type, but none of the comparison objects can accurately represent the observed near-IR fluxes of GJ 758 B. From comparison to atmospheric models, we attribute a $T_{\rm eff}$ = 600 ± 100 K, but we find that no atmospheric model can adequately fit all the fluxes of GJ 758 B. The lack of exploration of metal enrichment in model grids appears as a major limitation that prevents an accurate estimation of the companion physical parameters. The photometry of the new candidate companion is broadly consistent with L-type objects, but a second epoch with improved photometry is necessary to clarify its status. The new astrometry of GJ 758 B shows a significant proper motion since the last epoch. We use this result to improve the determination of the orbital characteristics using two fitting approaches: Least-Squares Monte Carlo and Markov chain Monte Carlo. We confirm the high-eccentricity of the orbit (peak at 0.5), and find a most likely semi-major axis of 46.05 AU. We also use our imaging data, as well as archival radial velocity data, to reject the possibility that this is a false positive effect created by an unseen, closer-in, companion. Finally, we analyze the sensitivity of our data to additional closer-in companions and reject the possibility of other massive brown dwarf companions down to 4–5 AU.

Key words. methods: data analysis – techniques: high angular resolution – techniques: image processing – stars: individual: GJ 758 – brown dwarfs

1. Introduction

The direct-imaging search for substellar companions around nearby stars has led to an increasing number of discoveries in the vicinity of our Sun. The brown dwarf companion, GJ 758 B (Thalmann et al. 2009), is one of t that stands out from the list. The primary star is a nearby (15.76%; van Leeuwen 2007) solar-type (G9V) star, and the inferred effective temperature ($T_{\rm eff}$) of GJ 758 B is among the lowest (~600 K) ever recorded for a directly imaged companion. These peculiarities made this system the subject of two separate studies (Currie et al. 2010; Janson et al. 2011) in addition to its discovery paper.

Previous observations have provided good spectral coverage of the GJ 758 system. Common proper motion of the companion with its parent star was determined through two epochs of Subaru/HiCIAO H-band observations detailed in Thalmann et al. (2009). In their work, they also highlight its very low $T_{\rm eff}$ (550–640 K) and late spectral type (T9). Currie et al. (2010) published MMT/Clio L'-band measurements of GJ 758 B. These data showed the object to have extremely red colors between near- and mid-infrared ($H - L' = 3.29 \pm 0.25$). The latest publication on GJ 758 B, by Janson et al. (2011), complete the spectral coverage with measurements in J, H, *CH4S*, *CH4L*, K_c, L' and M_s from Subaru/HiCIAO, Gemini/NIRI and Keck/NIRC2. They confirm again the very low $T_{\rm eff}$ and late spectral type of the companion and, for the first time, they demonstrate the clear methane absorption in H-band from the NIRI measurements in the *CH4S* and *CH4L* filters. In general, all three

⋆ Based on observations collected at the European Southern Observatory, Chile, during the commissioning of the SPHERE instrument.

Table 1. IRDIS DBI filter wavelengths and resolutions.

Filter pair	Filter	Wavelength (μm)	Resolution
Y23	*Y2*	1.022	20
	Y3	1.076	20
J23	*J2*	1.190	25
	J3	1.273	25
H23	*H2*	1.593	30
	H3	1.667	30
K12	*K1*	2.110	20
	K2	2.251	20

papers converge towards a similar picture of a low mass brown dwarf (30–40 $M_{\rm Jup}$), given the old age of the system (5–9 Gyr). First attempts at an orbit determination for GJ 758 B hinted at a large semi-major axis ($30 \leq a \leq 90$ AU) and high eccentricity ($0.4 \leq e \leq 0.7$). However, even though orbital motion is detected, further astrometric monitoring is needed for accurate orbital parameters to be determined. This is due to only a small fraction of the total orbit having been detected.

In this work we present new near-infrared (near-IR) photometric data obtained with the SPHERE instrument (Spectro-Polarimetric High-contrast Exoplanet REsearch; Beuzit et al. 2008), recently commissioned at the Very Large Telescope (VLT) in Chile. We first present our observations (Sect. 2), and the data reduction and analysis (Sect. 3). These new observations cover the full near-IR range at much higher contrast than previous observations, allowing us to detect a new candidate companion at a closer projected separation than GJ 758 B. We provide photometric measurements of GJ 758 B with improved sampling and resolution, including the very first measurements of the companion flux in *Y*-band. After revisiting the stellar parameters and age indicators for GJ 758 A (Sect. 4), we perform an updated modeling of the properties of GJ 758 B, making a comparison with empirical objects and atmospheric models (Sect. 5). Finally, we use the new astrometric datapoint to improve the orbit determination (Sect. 6) before concluding with our sensitivity to additional closer-in companions (Sect. 7).

2. Observations

The star GJ 758 was observed as part of the third SPHERE commissioning run in August 2014. The SPHERE planet finder instrument installed at the VLT (Beuzit et al. 2008) is a highly specialized instrument, dedicated to high-contrast imaging and spectroscopy of young giant exoplanets. It is based on the SAXO extreme adaptive optics system (Fusco et al. 2006; Petit et al. 2014; Sauvage et al. 2014), which controls a 41×41 actuators deformable mirror, and four control loops (fast visible tip-tilt, high-order, near-infrared differential tip-tilt, and pupil stabilization). The common path optics employ several stress polished toric mirrors (Hugot et al. 2012) to transport the beam to the coronagraphs and scientific instruments. Several types of coronagraphic devices for stellar diffraction-suppression are provided, including apodized pupil Lyot coronagraphs (Soummer 2005) and achromatic four-quadrants phase masks (Boccaletti et al. 2008).

The GJ 758 observations were acquired with one of the three scientific subsystems of SPHERE, the infrared dual-band imager and spectrograph (IRDIS; Dohlen et al. 2008) in its dual-band imaging mode (DBI; Vigan et al. 2010) with four different filter pairs in the *Y*-, *J*-, *H*- and $K_{\rm s}$-bands. The spectral characteristics of the filters are provided in Table 1. The observations were performed in pupil-stabilized mode to perform angular differential imaging (ADI; Marois et al. 2006) with an apodized pupil Lyot coronagraph (Soummer 2005) optimized for the *H*-band (ALC_YJH_S), which uses a coronagraphic mask of diameter 185 mas. The data were acquired on two consecutive nights, 13 and 14 August, 2014, with a total integration time of ~26 min in each filter pair. The IRDIS detector was dithered on a 4×4 pattern to reduce the effect of the residual flat-field noise. At each detector dithering position, a data cube of DIT × NDIT = 32 × 3 s was acquired, resulting in a total of 16 data cubes for each observation.

The observing sequence in each of the *DBI* filters was performed as follows:

- one image of the point spread function (PSF) taken off-axis (~0.4″) with the neutral density ND3.5, which reduces the flux by a factor ~3000. The PSF is moved off the coronagraph by applying an offset on the near-IR differential tip-tilt plate. During this observation, the AO visible tip-tilt and high-order loops remain closed to provide a diffraction-limited PSF;
- a "star center" coronagraphic image where four symmetric satellite spots are created by introducing a periodic modulation on the deformable mirror. This data is used in subsequent analysis to determine an accurate position of the star center behind the coronagraph, and hence the center of field rotation;
- the coronagraphic sequence as previously described;
- an additional off-axis PSF to evaluate the variations of the observing conditions between the beginning and end of the sequence.

For commissioning purposes, data from the SPARTA real-time computer of the SAXO extreme AO system (Fusco et al. 2014) were collected at regular intervals in parallel of all the observations. This includes, in particular, images from the differential tip-tilt sensor (DTTS). This sensor removes a minute fraction of the incoming flux in the near-IR arm (at 1.6 μm) to image the PSF just before the coronagraph, and uses it as input for the DTTS loop that maintains the PSF that is locked on the coronagraph, once the observing sequence has started. Every 30 s, the 30 s average of the non-coronagraphic PSF on the DTTS is saved in the SPARTA files, allowing a fine monitoring of the PSF motion and flux variation at the level of the coronagraph.

Standard calibrations for the DBI mode were acquired in the morning as part of the IRDIS calibration plan. Instrumental backgrounds were taken for both the coronagraphic and off-axis exposures with proper DIT values. Detector flat fields were also acquired in each of the *DBI* filter pairs.

3. Data reduction and analysis

The data were analyzed using two separate pipelines, which are described in this section.

The LAM-ADI pipeline is similar to that described in Vigan et al. (2012), after updates to work with the SPHERE/IRDIS data. The calibrations (backgrounds, flat) were created using the preliminary release (v0.14.0-2) of the SPHERE data reduction and handling (DRH) software (Pavlov et al. 2008). Each of the images in the coronagraphic observing sequences were background subtracted and divided by the flat field in the appropriate DBI filters. Bad pixels were corrected using bad pixel maps created with the DRH by replacing them with the median of neighboring good pixels. Finally, all images

Table 2. Observing log.

UT date	Julian date (day)	Filter pair	DIT[a] × NDIT (s)	Dithering[b]	T_{exp} (min)	FoV rot. (deg)	Seeing[c] (as)	Sr[c] (%)
2014-08-13	2 456 882	*J23*	32 × 3	4 × 4	25.6	7.1	0.50 ± 0.06	74 ± 4
2014-08-13	2 456 882	*H23*	32 × 3	4 × 4	25.6	7.2	0.58 ± 0.06	85 ± 2
2014-08-14	2 456 883	*Y23*	32 × 3	4 × 4	25.6	7.1	0.50 ± 0.11	58 ± 6
2014-08-14	2 456 883	*K12*	32 × 3	4 × 4	25.6	7.2	0.44 ± 0.05	89 ± 1

Notes. [(a)] Detector integration time. [(b)] Detector dithering (see text for details). NDIT images are acquired at each detector dithering position. [(c)] The seeing and Strehl ratio estimations are calculated over periods of 10 s every 30 s by the real-time computer. The Strehl ratio is expressed in the mean wavelength of the considered filter pair. The error bar is calculated as the standard deviation of the values.

were aligned to a common center using the star center data acquired at the beginning of the sequence. For this purpose, the four satellite spots inside the AO control radius were fitted with a 2D Gaussian function using the `MPFIT` non-linear least squares curve fitting software (Markwardt 2009). The accuracy of the centering using this procedure has been determined to be better than 0.1 pixel (∼1.2 mas) for bright stars during the first SPHERE commissioning run in May 2014. For the recentering of the science frames, the shift introduced by the detector dithering procedure was also taken into account, and the 0.06 pixel (0.74 mas) accuracy of the dithering motion stage was included into the astrometric error budget. For each filter pair, the calibration process was applied independently to each of the two wavelengths that were acquired simultaneously with IRDIS, resulting in two separate pre-processed ADI data cubes.

The ADI data cubes were processed with the LAM-ADI pipeline, using a principal component analysis (PCA) implementation following the Karhunen-Loève image projection (KLIP) approach (Soummer et al. 2012). The number of subtracted modes, minimum and maximum radii for the analysis were varied over a wide range, but the companion was recovered in all analyses. Figure 1 shows the signal of the companion in all of the IRDIS *DBI* filters. The companion is recovered in all filters with a signal-to-noise ratio (S/N) greater than six, except in the *K*2 filter where it is only marginally detected with an S/N of ∼2.5. As already presented in Janson et al. (2011), the companion displays a clear methane absorption in *H*-band with a flux about nine times fainter in *H3* than in *H2*. Images were also processed using a combination of spectral differential imaging (SDI; Racine et al. 1999) and ADI to attenuate the speckle noise even more and look for additional fainter candidates. In addition to the detection of GJ 758 B, we report the re-detection of the background star already identified by Janson et al. (2011), and the detection of a new candidate located ∼1.1″ south of the star in all filters except *K*2. Although not directly detectable in *H*2 and *H*3 with only ADI, the candidate was easily identifiable in the SDI+ADI processed image.

The precise astrometry and photometry of the companion and new candidate was estimated using "negative fake companion" subtraction in the pre-processed ADI data cubes (Marois et al. 2010). A rough estimation of the object position and contrast is first performed using a 2D Gaussian fit. Then these initial guesses are used as a starting point for a Levenberg-Marquardt least-squares minimization routine, where the position and contrast of the negative fake companion are varied to minimize the residual noise after ADI processing in a circular aperture of radius λ/D that is centered on the position of the companion. When a minimum is reached, the position and contrast of the fake companion are taken as the optimal values for the astrometry and photometry. We note that this procedure is also applicable for analyses combining SDI and ADI, by minimizing the residuals in an aperture that covers the position of the companion in the first filter, and in the second filter after spatial rescaling. The error bars for the fitting process are then calculated by varying the position and contrast of the fake companion until the variation of the reduced χ^2 reaches a level of 1σ.

The data were analyzed independently with the LESIA pipeline for a cross-check of the astrometry and photometry. This pipeline uses a similar approach for the pre-processing of the ADI data cubes, but for the speckles subtraction it uses an upgrade of the Template Locally Optimized Combination of Images (TLOCI) algorithm derived from the one presented in Marois et al. (2014). Only ADI is used (no SDI) to avoid issues with the photometry calibration (Maire et al. 2014). Hence, for each dual-band filter sequence, it calibrates the speckle pattern in each individual frame, rotates the frames to align North up, and median-combines all the frames to obtain the final image. To derive the photometry and the astrometry of the detected sources, the pipeline uses the unsaturated PSF of the central star (recorded before and after the coronagraphic sequence) to build a data cube composed of fake companions at the positions of the detected sources that account for the field-of-view rotation in each frame and smearing during exposures. Then, the frames of this data cube are combined using the TLOCI coefficients that were used to obtain the image where the point-source was detected. The resulting frames are aligned in the same way as the science data to obtain an image that gives a model of the off-axis sources in the TLOCI images at the positions of the detections, accounting for TLOCI self-subtraction and distortions. Finally, the sub-pixel position and the flux of the modeled images are adjusted to optimize the subtraction of the model to the real image within a 1.5 λ/D-radius disk centered on the detection (Galicher & Marois 2011). The error bars account for the variations of the stellar flux during the sequence (estimated from the global speckle intensity variations), and the accuracy of the fitting of the companion image models to the real images.

For calibrating the distortion, plate scale, and orientation of the IRDIS images, a field in the outer regions of the 47 Tuc globular cluster was observed in different instrumental configurations (Maire et al. 2016). The 47 Tuc field was selected because it includes a bright star for adaptive optics guiding and was accurately calibrated using *Hubble* Space Telescope (HST) observations (Bellini et al. 2014). The plate scales for the different DBI filters are summarized in Table 3. Since it was not calibrated in the *K*12 filter pair during the commissioning, we assumed the same value as for the *H*23 filter pair. The true North correction measured for this commissioning run is −1.636 ± 0.013 deg, and the correction of the orientation also takes into account the zero point orientation of the derotator in pupil-stabilized mode, which was measured to be 135.87 ± 0.03 deg.

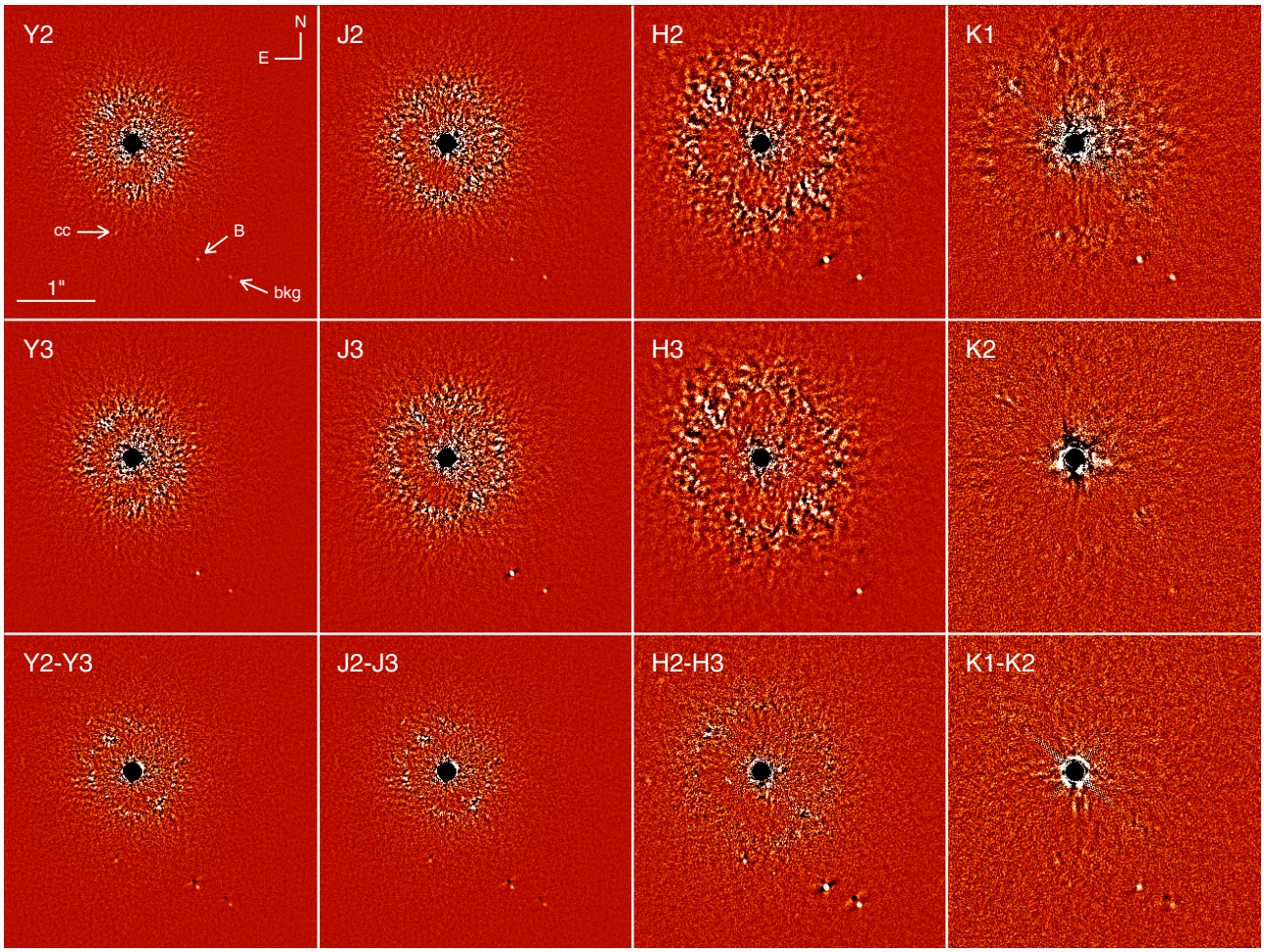

Fig. 1. Images of GJ 758 after ADI and SDI processing in all IRDIS *DBI* filters. For each filter pair, *the top and middle rows* present the ADI analysis of the data in the first and second filters respectively, and *the bottom row* presents the result of the SDI+ADI analysis. For the ADI analysis, five PCA modes were subtracted, while for the SDI+ADI analysis, only a single mode was subtracted. Three objects are clearly identified in the data: GJ 758 B (B), a background star (bkg) and a new candidate companion (cc). The spatial and display scales are identical between all images. The SDI images display the characteristic negative/positive pattern expected for physical objects that present flux in both *DBI* filters. For the highly methane-bearing object GJ 758 B, the flux difference between the $H2$ and $H3$ filters is clearly visible.

Relative photometry and astrometry of the companion and the newly detected candidate are reported in Table 4. Both pipelines agree within their respective error bars. The values reported in the table correspond to the average of the results from both pipelines, and the respective error bars have been quadratically added. The final error bars for the photometry include the fitting error detailed above, the variation of the non-coronagraphic PSF measured on the DTTS images (see Sect. 2), and the level of speckle residuals estimated at the same separation as the detections. The astrometric error bars include the fitting error, and the uncertainties on the star center, dithering motion, plate scale, derotator zero point, and true North correction. We note that for astrometry, the reference values are those from the $H23$ filter pair, which has been the most accurately calibrated.

Table 3. Mean plate scale measured from observations of the 47 Tuc globular cluster.

Filter	Plate scale (mas/pixel)
Y2	12.287 ± 0.006
Y3	12.282 ± 0.006
J2	12.267 ± 0.006
J3	12.262 ± 0.006
H2	12.263 ± 0.006
H3	12.258 ± 0.006

4. Stellar parameters

A reassessment of stellar parameters of GJ 758 is warranted, when taking their relevance in the derivation of the properties of its substellar companion into consideration, and to explain its peculiar features discussed in Sect. 5. The star GJ 758 is classified as old (age 0.7–8.7 Gyr; Janson et al. 2011), and we revisit here the various age indicators, following the procedures and calibrations described in Desidera et al. (2015), as well as the chemical composition.

4.1. Kinematic parameters

Adopting the trigonometric parallax, the proper motion and error bars by van Leeuwen (2007), and the absolute radial velocity by Nidever et al. (2002) with an error of 0.50 km s^{-1}, space velocities $U, V, W = -21.1 \pm 0.2; -14.1 \pm 0.5; -3.0 \pm 0.2$ km s^{-1} are

Table 4. Astrometry and photometry of GJ 758 B and the newly detected candidate relative to primary

Filter	$\Delta\alpha$ (mas)	$\Delta\delta$ (mas)	Sep. (mas)	PA (deg)	Δmag (mag)
			GJ 758 B		
Y2	-793 ± 4	-1501 ± 3	1698 ± 3	207.85 ± 0.13	14.90 ± 0.19
Y3	-789 ± 4	-1501 ± 2	1698 ± 2	207.86 ± 0.12	14.20 ± 0.09
J2	-789 ± 4	-1499 ± 4	1694 ± 4	207.77 ± 0.16	14.97 ± 0.24
J3	-789 ± 4	-1499 ± 2	1694 ± 2	207.78 ± 0.12	12.89 ± 0.17
H2	-791 ± 4	-1501 ± 2	1697 ± 2	207.80 ± 0.12	12.95 ± 0.11
H3	-792 ± 7	-1500 ± 7	1696 ± 7	207.83 ± 0.24	15.29 ± 0.41
K1	-784 ± 7	-1500 ± 8	1692 ± 8	207.58 ± 0.25	13.46 ± 0.20
K2	-794 ± 12	-1508 ± 12	1704 ± 12	207.76 ± 0.50	14.21 ± 0.34
			New candidate companion		
Y2	239 ± 6	-1132 ± 12	1156 ± 12	168.09 ± 0.31	15.45 ± 0.62
Y3	241 ± 7	-1133 ± 11	1158 ± 11	168.00 ± 0.35	14.40 ± 0.86
J2	242 ± 6	-1141 ± 12	1167 ± 12	168.04 ± 0.31	14.67 ± 0.60
J3	244 ± 10	-1137 ± 19	1163 ± 18	167.89 ± 0.51	15.01 ± 0.92
H2[a]	240 ± 8	-1139 ± 9	1164 ± 9	168.11 ± 0.40	14.67 ± 0.61
H3[a]	...	...	...	...	14.64 ± 0.61
K1	263 ± 13	-1157 ± 20	1187 ± 19	167.18 ± 0.65	13.77 ± 0.30

Notes. [(a)] The *H23* photometry and astrometry of the new candidate companion are determined jointly using a combination of SDI and ADI (see text for details). In this context, the astrometry is only relevant in the *H2* filter.

obtained. These are very similar to those of the Argus association ($U, V, W = -21.5 \pm 0.9, -12.2 \pm 1.7, -4.6 \pm 2.7$). Although the `BANYAN II` on-line tool (Gagné et al. 2014) yields a membership probability of 97.8%, which would correspond to a very young age of 40 Myr, the full version of the `BANYAN I` tool (Malo et al. 2013), which takes into account both kinematic and photometric information, yields a 100% probability to the hypothesis that GJ 758 is an old field star.

4.2. Abundance analysis

We determined spectroscopic stellar parameters and chemical abundances for GJ 758 by exploiting a high-resolution (R = 42 000), high S/N (S/N = 164 at 5500 Å) ELODIE spectrum[1], which provides a wavelength coverage from 3850 Å to 6800 Å. The spectrum was downloaded from the online ELODIE archive (Moultaka et al. 2004), which provides reduced data products. This investigation aims at chemically tagging our target star, to ascertain whether the abundance pattern is compatible with the Argus association, whose chemical composition has been recently presented by De Silva et al. (2013). Argus reflects a roughly solar chemical composition with [Fe/H] = -0.06 ± 0.05 dex and all [X/Fe] ratios within 0.15 dex from the solar values, with the notable exception of barium (see discussion below).

We carried out a homogeneous and strictly differential analysis for GJ 758 with respect to Argus members published in that previous work by utilizing the same code (MOOG by Sneden 1973, 2014 version), line lists, techniques, and grid of model atmospheres (Kurucz 1993, solar-scaled models and no convective overshooting). Effective temperature ($T_{\rm eff}$) and surface gravity ($\log g$) were derived by imposing excitation and ionisation equilibrium, so that there is no spurious trend of A(Fe) with the excitation potentials of the spectral features and agreement (within 0.05 dex) of iron abundances from Fe I and Fe II, respectively. Instead, the microturbulence velocity (ξ) was calculated requiring that abundances from Fe I lines show no trend with reduced equivalent widths. We performed equivalent width analysis for Fe, Na, Mg, Al, Si, Ca, Ti, Cr, and Ni, whereas the Ba abundance was inferred via spectral synthesis, including hyperfine structure and isotopic splitting (see De Silva et al. (2013).

Table 5. Spectroscopic stellar parameters and abundances for GJ 758.

$T_{\rm eff}$ (K)	5498 ± 50
$\log g$ (cm s^{-2})	4.53 ± 0.10
ξ (km s^{-1})	1.12 ± 0.10
[Fe/H]I	0.18 ± 0.05
[Fe/H]II	0.13 ± 0.08
[Na/Fe]	0.12 ± 0.05
[Mg/Fe]	0.11 ± 0.05
[Al/Fe]	0.12 ± 0.05
[Si/Fe]	0.01 ± 0.05
[Ca/Fe]	0.03 ± 0.03
[Ti/Fe]I	0.09 ± 0.05
[Ti/Fe]II	0.07 ± 0.08
[Cr/Fe]I	0.03 ± 0.05
[Cr/Fe]II	0.07 ± 0.06
[Ni/Fe]	0.04 ± 0.03
[Ba/Fe]II	0.00 ± 0.12

Internal (random) uncertainties affecting our derived abundances were computed in the standard way, that is by adding in quadrature errors resulting from the equivalent-width (EW) measurements (or to the best-fit determination in the case of spectral synthesis) and those related to the adopted set of atmospheric parameters ($T_{\rm eff}$, $\log g$, and ξ). The total internal errors for [Fe/H], as well as for [X/Fe] ratios, are given in Table 5 (see De Silva et al. 2013 for further details on the error budget calculation).

We found a metallicity of [Fe/H] = 0.18 ± 0.05, which agrees very well with previous determinations by e.g., Soubiran et al. (2008), Takeda (2007), and Maldonado et al. (2012) and points to super-solar heavy element abundances for this star. The abundances of α-elements Si and Ca, as well as the Fe-peak Cr and Ni, match a solar-scaled pattern, whereas Na, Mg, Al, and Ti (though to a less extent) seem to exhibit a modest

[1] http://atlas.obs-hp.fr/elodie/fE.cgi?c=o\&o=GJ758

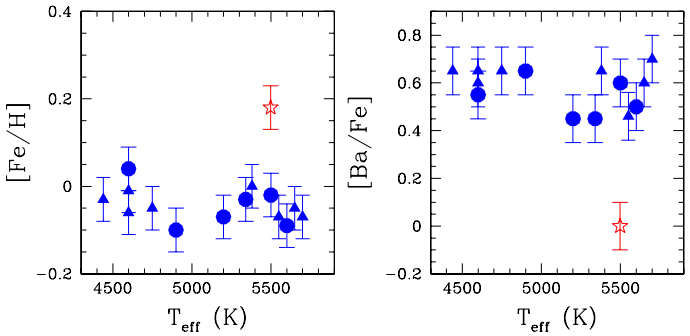

Fig. 2. Fe and Ba abundances versus effective temperatures for GJ 758 (starred symbol), the Argus association and the open cluster IC 2391 (triangles and circles, respectively, from De Silva et al. 2013).

enhancement, albeit still consistent with solar abundances within the observational uncertainties. The metallicity distribution as a function of effective temperatures is shown in the left-hand panel of Fig. 2: we report [Fe/H] values for GJ 758 along with stars belonging to Argus (filled circles) and to the open cluster IC 2391 (triangles), deemed to share a common origin with the young association. It is clear from Fig. 2 that GJ 758 stands out from the cluster/association distribution, with its [Fe/H] being roughly ∼0.25 dex higher.

Barium deserves a brief, separate discussion. First identified by D'Orazi et al. (2012), and subsequently confirmed by several studies (e.g., Yong et al. 2012; Jacobson & Friel 2013; Mishenina et al. 2013), the Ba abundance shows a decreasing trend with the open cluster's age. The younger the cluster, the higher its Ba content. The reason for such a peculiar and unique pattern is still a matter for debate: it has been suggested that the efficiency in the production of the *s*-process elements in low-mass AGB stars is higher than that predicted for standard stellar evolution models, and input physics has still to be revised (D'Orazi et al. 2009; Maiorca et al. 2012). However, subsequent investigations show that the picture might not be that straightforward. The fact that the Ba overabundance is not accompanied by a similar behavior in other *s*-process elements (e.g., Y, La) makes this explanation unlikely. We refer the reader to (D'Orazi et al. 2012) for a wider discussion of this topic. Regardless of the nature of the super-solar Ba content, [Ba/Fe] ratios range from extremely high values of approximately ∼0.6 dex for pre-main sequence clusters, such as e.g., IC 2602 and IC 2391 (D'Orazi & Randich 2009) to solar values, or even lower, for clusters a few Gyr old. De Silva et al. (2013) corroborated this observational evidence and obtained a mean abundance of [Ba/Fe] = 0.53 ± 0.03 (rms = 0.08 dex) for the Argus association and [Ba/Fe] = 0.62 ± 0.02 (rms = 0.07) for IC 2391 (see the right-hand panel of Fig. 2). Conversely, we gathered a [Ba/Fe] = 0.00 ± 0.12 for our star, which implies a difference in the Ba content of more than a factor of 3.5. Thus, in terms of chemical composition, Ba provides us with the strongest observational constraint: GJ 758 cannot have been born from the same molecular cloud as Argus.

4.3. Age indicators

The star, GJ 758, is known to have a low activity level that results from several measurements in the literature: $\log R_{\rm HK}$ = −4.94 (Wright et al. 2004), −5.015 (Isaacson & Fischer 2010); and −5.060 (Duncan et al. 1991; Mamajek & Hillenbrand 2008). The calibration by Mamajek & Hillenbrand (2008) yields values of 5.5–7.7 Gyr for these activity values. The availability of multi-epoch measurements of chromospheric activity spanning several years indicate that this is not the result of a poor sampling of an activity cycle. The X-ray non-detection in the ROSAT All Sky Survey (Voges et al. 1999, 2000) (which would imply $\log L_{\rm X}/L_{\rm bol} < -5.8$ and then an age > 3 Gyr), the small projected rotational velocity (0–2 km s^{-1}), and the small photometric variability (0.008 mag from HIPPARCOS) further support the low activity level of GJ 758, as expected for a few-Gyr old star.

Lithium is another highly sensitive age indicator for young stars. From the analysis of the spectrum described in Sect. 4.2, the Li 6708 Å resonance line is not detected, confirming the null result by Takeda & Kawanomoto (2005). For stars with GJ 758 colors, detectable amounts of lithium vanish at about the age of the Hyades. Therefore, the lack of lithium allows us to infer a stellar age that is older than 600 Myr.

While stellar members of young moving groups display significant scatter in the age indicators (see Desidera et al. 2011, for the case of Argus), we are not aware of late G-type stars, which are confirmed members of young moving groups, and which have such a low activity level and lack of lithium. The analysis of these indicators therefore converges with the chemical tagging in ruling out Argus membership for GJ 758.

Using the spectroscopic effective temperature and metallicity, and the HIPPARCOS *V* magnitude and trigonometric parallax, we derive age and masses from isochrone using the PARAM interface (da Silva et al. 2006)[2] and the stellar models by Bressan et al. (2012). Limiting possible input values to an age larger than 0.6 Gyr, the result of a lack of lithium, the resulting age would be 2.2 ± 1.4 Gyr and the stellar mass 0.97 ± 0.02 $M_{\odot}$.

4.4. Summary

All age indicators suggest that GJ 758 is an old star with lithium providing a tight lower limit at 600 Myr. Chemical tagging derived from a homogeneous comparison of abundances of several elements with those of confirmed members of the Argus association and IC 2391 open cluster also rules out a link between GJ 758 and Argus, with Barium abundance suggesting an age similar to the Sun. Therefore, we conclude that the kinematic parameters of GJ 758 are similar to those of the Argus association by chance, which confirmsing the statistical nature of kinematic ages and the need for independent youth indications to conclusively infer membership in young moving groups (Gagné et al. 2014; Desidera et al. 2015). The young disk kinematics decrease the probability of a star being significantly older than the Sun. The age of the system is likely to be within one to six Gyr, and the most probable value around three Gyr, with isochrone fitting yielding younger values than chromospheric activity. We also confirm the moderate super-solar metallicity of the star.

5. Spectrophotometric analysis

The new SPHERE photometry is complementary to the existing set of photometric data points on the spectral energy distribution (SED) of the companion obtained by Janson et al. (2011). In the following we use the more complete SED to refine the properties of GJ 758 B.

[2] http://stev.oapd.inaf.it/cgi-bin/param

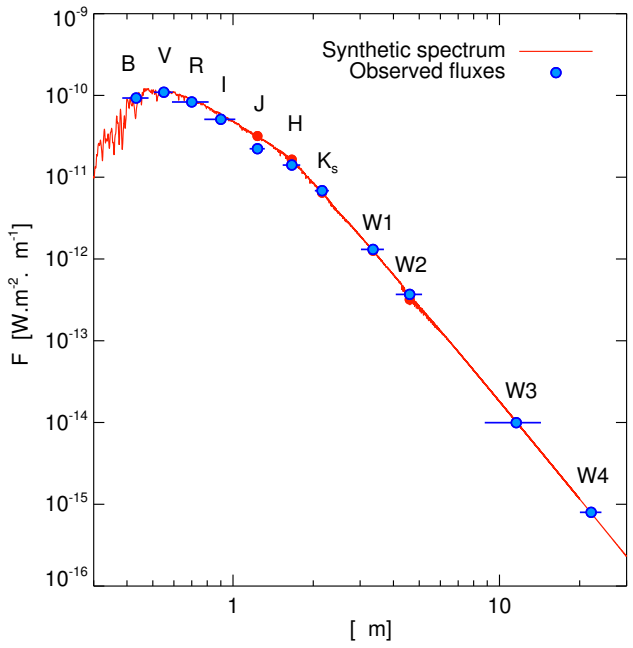

Fig. 3. *Gaia*-COND synthetic spectrum adjusted to the spectral energy distribution of GJ 758 A and built from a compilation of optical, near-infrared, and mid-infrared photometry. The 2MASS J, H, K_s, and WISE *W1*-*W2* photometry data were excluded from the fit because the star was saturating in the 2MASS images.

5.1. Fluxes and magnitudes

We retrieved the apparent fluxes that correspond to the SPHERE/IRDIS photometry of the companion by using the contrast ratio listed in Table 4 and by following a three-step process:

- We first built the 0.4–22.1 μm SED of the star from the Tycho B_T, V_T (Hoeg et al. 1997), USNO-B R, and I (Monet et al. 2003), and WISE *W3*-*W4* photometry (Cutri et al. 2013). The 2MASS J, H, K_s, (Cutri et al. 2003) and *W1*-*W2* photometry could not be used because of the saturation of the star (see Janson et al. 2011). The optical photometry was converted to apparent fluxes using the Gemini flux-conversion tool[3]. We considered the WISE zero points reported in Jarrett et al. (2011) for the infrared part.
- We adjusted a *Gaia*-COND model (Brott & Hauschildt 2005) with $T_{\rm eff}$ = 5400 K, log g = 4.0 dex, and M/H = 0.0 to GJ 758 A fluxes values. This model has atmospheric parameters close to the ones determined from high-resolution spectra of the star ($T_{\rm eff}$ = 5435 K, log g = 4.0, M/H = 0.12; Kovtyukh et al. 2004). The *Gaia* model reproduces the SED of GJ 758 (Fig. 3) well, including the 2MASS K_s band photometry, which appears to be less affected by the saturation.
- We derived the mean stellar flux into the SPHERE/IRDIS passbands using the flux-calibrated *Gaia* spectrum and the tabulated filter widths reported in Table 1.

The remaining fluxes of GJ 758 B were estimated directly from a flux-calibrated spectrum of Vega (Bohlin 2007), the Keck/NIRC2 and Gemini/NIRI magnitudes of the companions reported in Janson et al. (2011), and corresponding filter transmission curves. The effect of the telluric absorption on the final flux estimates for the companion was simulated using the ESO sky model calculator[4] (Noll et al. 2012; Jones et al. 2013). We considered two altitudes of targets above the horizon (90 and 30°) to simulate dry and wet conditions. The effect is found to be negligible, compared to the error in the companion photometry. The final estimated fluxes of GJ 758 B, which we consider for the following analysis, are reported in Table 6. The fluxes in the overlapping narrow-band *K1* and K_c filters are almost identical. This is an indication that our flux-conversion methods yield consistent results.

[3] http://www.gemini.edu/sciops/instruments/midir-resources/imaging-calibrations/fluxmagnitude-conversion

Table 6. Apparent fluxes of GJ 758 B.

Filter	λ (nm)	$\Delta\lambda$ (nm)	F_λ (W m^{-2} μm^{-1})	ΔF_λ (W m^{-2} μm^{-1})	Ref.
Y2	1022	51	5.074×10^{-17}	9.703×10^{-18}	1
Y3	1076	54	8.526×10^{-17}	7.368×10^{-18}	1
J2	1190	48	3.449×10^{-17}	8.532×10^{-18}	1
J	1250	180	1.126×10^{-16}	2.280×10^{-17}	2
J3	1273	51	2.070×10^{-16}	3.508×10^{-17}	1
CH4S	1580	103	4.074×10^{-17}	8.240×10^{-18}	2
H2	1593	53	1.177×10^{-16}	1.255×10^{-17}	1
H	1650	290	2.536×10^{-17}	5.130×10^{-18}	2
H3	1667	56	1.222×10^{-17}	5.605×10^{-18}	1
CH4L	1690	110	$\leq 1.457 \times 10^{-17}$	...	2
K_c	2098	28	2.747×10^{-17}	5.550×10^{-18}	2
K1	2110	105	2.897×10^{-17}	5.859×10^{-18}	1
K2	2251	112	1.145×10^{-17}	4.209×10^{-18}	1
L'	3776	700	2.163×10^{-17}	2.090×10^{-18}	2
M_s	4670	241	$\leq 5.257 \times 10^{-17}$	...	2

References. (1) This work; (2) Janson et al. (2011).

5.2. Comparison of GJ 758 B to empirical objects

The *Y3*/*J2*, *J2*/*J3*, *H2*/*H3*, and *K1*/*K2* flux ratios provide a clear detection of water and methane absorptions around 1.15, 1.6, and 2.3 μm in the atmosphere of the brown-dwarf companion. We compared its 1–2.5 μm SED to those of 101 T0–T8 field dwarfs with near-infrared spectra taken from the SpeXPrism library (Burgasser 2014). The mean flux $F_{k,i}$ and error $\sigma_{F_{k,i}}$ associated with each template spectrum k and filter passband i was estimated and compared to the companion SED f and error σ_f using the G'' goodness-of-fit indicator defined by Bowler et al. (2010):

$$G''_k = \sum_{i=1}^{n} w_i \frac{(f_i - C''_k F_{k,i})^2}{\sigma_{f_i}^2 + (C''_k \sigma_{F_{k,i}})^2}, \quad (1)$$

where C''_k is a renormalization factor applied to the template SED k, which minimizes G''_k. w_i is the renormalized FWHM $\Delta\lambda_i$ of each filter i following

$$w_i = \frac{\Delta\lambda_i}{\sum_{j=1}^{n} \Delta\lambda_j}. \quad (2)$$

The indicator enables us to compare SEDs with an inhomogeneous wavelength sampling and with measurement errors on both the templates and the object. We rejected solutions which exceeded the upper limit of the flux into the *CH4L* passband (Janson et al. 2011). The G'' indicator is minimized for the

[4] https://www.eso.org/observing/etc/bin/gen/form?INS.MODE=swspectr+INS.NAME=SKYCALC

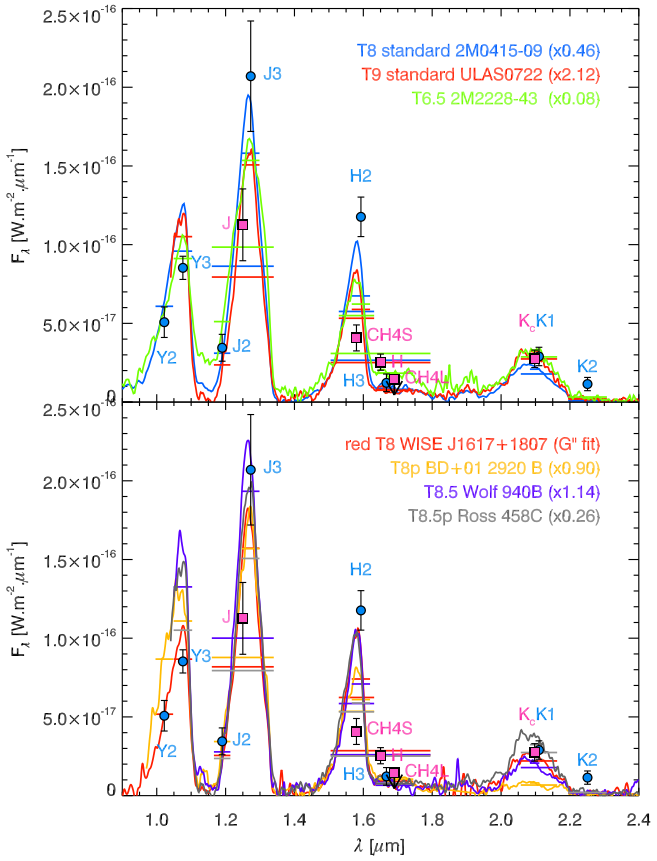

Fig. 4. Comparison of the 1–2.5 μm spectral-energy distribution of GJ 758 B to those of T8, T9 standard, benchmark companions, and to the red T8 dwarf WISEJ1617+1807 (Burgasser et al. 2011). The large blue circles represent our new IRDIS measurements, while the large pink squares represent the measurements from Janson et al. (2011). The horizontal lines correspond to the expected fluxes of the empirical objets in each filter bandpass.

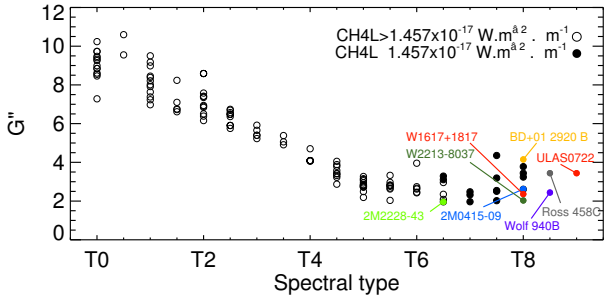

Fig. 5. G'' values inferred from the comparison of SEDs of T dwarfs (generated from SpecXPrism spectra) with the SED of GJ 578 B. The re-normalized SEDs, whose flux in the *CH4L* passband respect the upper limit set for GJ 758 B, are reported as filled dots. Those which do not are shown as open circles. The G'' values for the objects considered in Fig. 4 are overlaid. We also report the value for the red T8 dwarf WISEP J231336.41-803701.4, whose SED, along with the one of the red T8 WISEP J161705.75+180714.0, provide the best visual fits to the SED of the companion.

Table 7. Absolute magnitudes of GJ 758 A, GJ 758 B, and of the candidate companion estimated from the contrast ratio and the model spectrum of the star.

Filter	GJ 758 A[a]	GJ 758 B	New c.c.
Y2	4.29 ± 0.03	19.19 ± 0.20	19.74 ± 0.62
Y3	4.23 ± 0.03	18.43 ± 0.10	18.73 ± 0.86
J2	4.09 ± 0.03	19.06 ± 0.25	18.76 ± 0.60
J3	3.94 ± 0.03	16.83 ± 0.18	18.95 ± 0.92
H2	3.64 ± 0.03	16.59 ± 0.12	18.31 ± 0.61
H3	3.59 ± 0.03	18.88 ± 0.42	18.23 ± 0.61
K1	3.58 ± 0.03	17.03 ± 0.21	17.35 ± 0.62
K2	3.57 ± 0.03	17.78 ± 0.35	...

Notes. [(a)] 0.03 mag uncertainty assumed, based on the SED fit of GJ 758 A and on the error in the available optical+WISE photometry of the star.

T6.5 dwarf 2MASS J22282889-4310262 (Burgasser et al. 2004), which is known to experience wavelength-dependent photometric variability (Buenzli et al. 2012). The comparison is shown in the upper panel of Fig. 4, and we report the G'' values as a function of spectral type in Fig. 5. When flux-calibrated and scaled to the distance of GJ 758 B (using the parallax of Faherty et al. 2012), the spectrum of 2MASS J22282889-4310262 is over-luminous and a multiplication factor of 0.08 must be applied to fit the companion SED. This indicates that GJ 758 B is most likely later than T6.5. The variation of G'' with the spectral type also clearly confirms that the companion is later than T5. This agrees with the conclusions of Janson et al. (2011).

In the lower panel of Fig. 4, we show the spectra of standard T8 and T9 dwarfs (Burgasser et al. 2004; Lucas et al. 2010) with measured trigonometric parallaxes and fluxes brought to the distance of the GJ 758 system. The companion SED is midway between the renormalized SED of the T8 and T9 standards. Nevertheless, the templates fail to reproduce the *J3*, *H2*, and *K2* fluxes simultaneously. The companion also appears to have a luminosity intermediate between these two objects. Its *J*- and *H*-band absolute magnitudes agree well with the mean values reported in Dupuy & Kraus (2013) for T8-T8.5 objects.

The causes of the peculiar SED of GJ 758 B are unclear. The companion spectrophotometric properties could be related to a non-solar composition, or a surface gravity that is different to those of standard T8-T9 dwarfs. Both parameters produce opposite effects on 1–5 μm SEDs that are difficult to disentangle (e.g. Leggett et al. 2010). We used the spectra of wide companions to stars with a known age and metallicity to investigate the effect of peculiar atmospheric parameters, making the assumption that these objects share the same composition as their host star.

Ross 458 C (Goldman et al. 2010; Scholz 2010) appears as the only object with an estimated age (150–800 Myr) that is younger than the typical field dwarf ages (≫500 Myr), which has an estimated $T_{\rm eff}$ (625–755 K Burgasser et al. 2010; Burningham et al. 2011) and near-infrared spectral type (T8.5p) in the same range as that of GJ 758 B (Janson et al. 2011). It is also reported to have a super-solar metallicity (Fe/H = +0.2–0.3; Burgasser et al. 2010), e.g., similar to that of GJ 758 A (+0.2 dex, see Sect. 4). The spectra of both objects are also compared in the lower panel of Fig. 4. The spectrum of Ross 458 C from Burningham et al. (2011) represents the SED of GJ 758 B less well than the T8 standard. Its enhanced flux at *K*-band suggests that the two companions do not span the same surface gravity and/or metallicity interval.

We considered the opposite case of the peculiar T8 companion to the metal-poor ([Fe/H] = −0.38 ± 0.06 dex) G-type star BD+01 292 (Pinfield et al. 2012) and of the T8 companion to the sdM1.5+WD binary Wolf 1130 ([Fe/H] = −0.64 ± 0.17).

Table 8. Fitting solutions with the highest f_{MC} values for the GJ 758 B SED and the three sets of atmospheric models using the G goodness-of-fit indicator.

Model	T_{eff}	log g	[M/H]	[α]	f_{SED}	R	G	f_{MC}
BT-SETTL14-Y	700	3.5	0.0	0.0	n/a	0.60	1.80	0.55
BT-SETTL14	650	5.0	0.0	0.3	n/a	0.71	1.60	0.20
Exo-REM–NC	500	5.5	0.0	0.0	n/a	1.26	4.83	0.85
Exo-REM–T3	500	5.5	0.0	0.0	n/a	1.26	4.83	0.63
Morley+12	600	4.5	0.0	0.0	5.0	0.91	1.39	0.30
Saumon+12	600	5.5	0.0	0.0	n/a	0.85	2.70	0.74

Both companions have a suppressed flux at K-band, possibly due to the enhanced collision-induced absorption of H_2 encountered into clear/low-metallicity/higher-pressure atmospheres (Saumon et al. 1994; Borysow et al. 1997). They clearly produce a worse fit to the SED of GJ 758 B than the T8 standard does. In summary, we see an opposite trend for GJ 758 B's departure from the SED of the standard T8.

The T8.5 companion to the old (3.5–6 Gyr) solar-metallicity star Wolf 940 (Burningham et al. 2009, [Fe/H] = −0.06 ± 0.20) represents the J-band flux better, at the price of a degradation in the fit in the Y band. We do not find a good fit with earlier type companions such as GJ 229 B (T7pec) or Gl 570 D (T7.5) (Geballe et al. 1996, 2001) nor primaries with roughly solar-metallicities (Neves et al. 2014).

We extended the comparison to additional peculiar dwarfs with red near-IR colors but no a priori knowledge of their age and metallicity (e.g. Mace et al. 2013, and references therein). We find that the red T8 dwarfs WISEP J161705.75+180714.0 and WISEP J231336.41-803701.4 (Burgasser et al. 2011) provide the best fit among all other aforementioned objects. They notably represent the Y-band flux well, compared to the other objects. Burgasser et al. (2011) note that the spectral properties of these two objects suggest cool (T_{eff} = 600 K), low surface gravity (log g = 4.0), and cloudy atmospheres.

In summary, we cannot find an empirical object with known metallicity and distance that accurately represents all the near-IR narrowband and broadband fluxes of GJ 758 B simultaneously. We estimate a T8 spectral type from this comparison. The analysis is, however, certainly limited by the small amount of spectra of T8–T9 dwarfs with robust constraints on their age and metallicity.

5.3. Comparison of GJ 758 B to atmospheric models

We compared the SED of GJ 758 B to four sets of atmospheric models, i.e. BT-Settl, Exo-REM, Morley+12, and Saumon+12, in order to refine the estimate of log g, T_{eff}, and Fe/H, and to understand its peculiar photometry. The models are described in Allard et al. (2013), Baudino et al. (2015), Morley et al. (2012), and Saumon et al. (2012) respectively. The specificities and parameter space of the models are described in more detail in Appendix A and Table A.1. We expect that the use of these different classes of models will allow the best possible approach for the accurate modeling of the atmospheric parameters.

To account for the inhomogeneous sampling of the real SED during the fitting process, we decided to use the goodness-of-fit G_k indicator defined by Cushing et al. (2008). This indicator contains a dilution factor, C_k, similar to the C_k'' factor defined in Eq. (1). C_k usually equals $(R/d)^2$, where d is the distance of the source and R its radius. Given the HIPPARCOS distance from GJ 758 A, we were able to retrieve the optimal average object radii for each given model.

Confidence levels cannot be derived directly from G. Therefore, we followed the approach of Cushing et al. (2008) to determine the most meaningful fitting solution for each model grid. For each photometric data point of the object, we generated a normal Monte-Carlo (MC) distribution of 10 000 draws with mean values of f_i and standard deviations of σ_i. The G_k values were computed for each of the resulting 10 000 SEDs. For each model of the grid, we computed the fraction of the 10 000 MC simulated SEDs that were best fitted by this given model. This f_{MC} indicator, ranging from 0 to 1, enabled us to test the significance of any fitting solution. The models with the highest f_{MC} value represents the most significant solution. However, we note that f_{MC} is sensitive to the sampling and extent of the model grid. Therefore, despite the criterion being useful for estimating the robustness of a given solution within a grid, it should not be used to evaluate the quality of the solutions found with different grids. We performed a visual inspection of the three solutions with the highest f_{MC} for each model grid, but only reported the atmospheric parameters and f_{MC} of the most probable solution in Table 8.

The Monte Carlo method works as long as the errors associated with f_i are uncorrelated. In the case of GJ 758 B, the errors associated with the flux-calibrated SED of the object combine uncorrelated errors. These correspond with companion contrast values that are associated with each filter to a correlated error, which arises for the flux-calibrated spectrum of the star. We accounted for both sources of errors in our MC simulations by multiplying the 10 000 MC SEDs of the companion by $10^{-0.4 \times N(\mu=0,\sigma_{ph})}$ with N an additional MC normal distribution. From this distribution, 10 000 values were drawn with mean values of 0 and a standard deviation σ_{ph} equal to the magnitude error on the flux-scaling of the companion spectrum. We took σ_{ph} = 0.03 mag, which corresponds to the highest photometric error on the SED of the star.

The results of the fits are reported into Table 8 and shown in Fig. 6. The solutions with the highest f_{MC} always correspond to the solution with the minimum G. The corresponding dilution factors inferred from our MC simulations for the most probable fitting solution (highest f_{MC}) are shown in Fig. 7. No one model represents the whole SED well, especially the J3 and H2 fluxes. The Morley+12 models provide the best fits according to the G indicator. The three most significant solutions (>65% of the solutions) found with these models correspond to log g = 4.0–4.5 and T_{eff} = 550–600 K. The cloud-free Saumon+12 models only provides a better fit to the J-band flux. But their poorer representation of the other bands indicate that clouds are still needed in the photosphere to reproduce the GJ 758 B SED. Visually, the BT-SETTL14 models seem to provide a better fit to the H-band flux. The flux drop at M_s band in the BT-SETTL14 models is in better agreement with the upper limit found by Janson et al. (2011). New deeper observations at the M-band of the GJ 758 system could help to further discriminate the models.

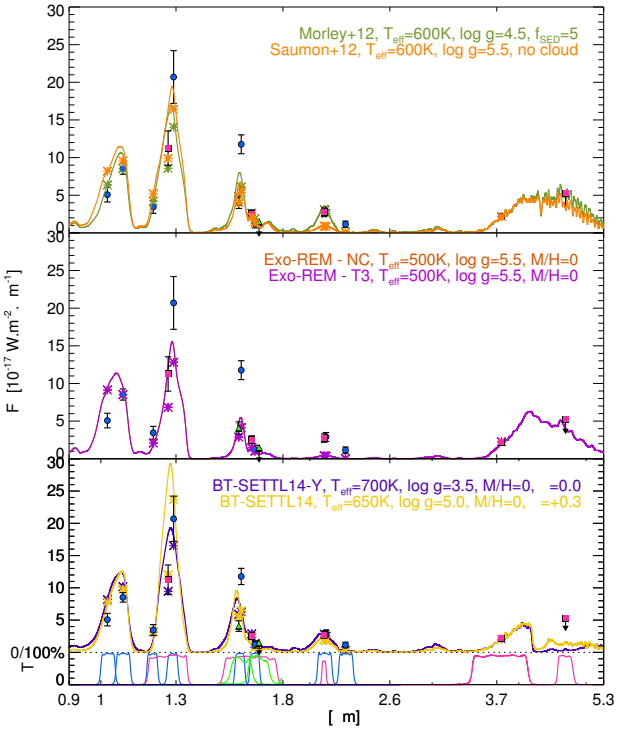

Fig. 6. Comparison of the 1–5 μm spectral-energy distribution of GJ 758 B to the best fitting synthetic spectra from the BT-SETTL14, Morley+12, Saumon+12, and Exo-REM grids. The asterisks represent the expected fluxes in each bandpass from the atmospheric models. The Exo-REM and Exo-REM – NC models completely overlap because, at this combination of $T_{\rm eff}$ and log g, the cloud condensation occurs below the considered pressure grid, effectively making both models cloud-free.

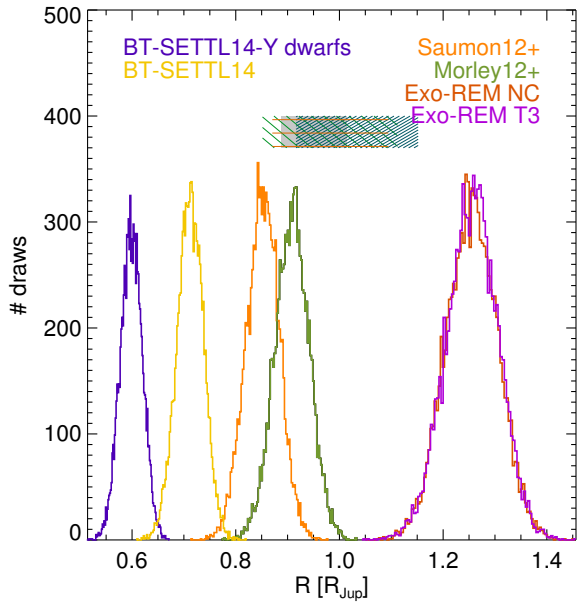

Fig. 7. Histogram of radii (dilution factors C_k, directly related to radius because the distance is known) derived from the comparison of the most frequent best-fitting solution for each Monte-Carlo simulation of the SED of GJ 758 B. The hatched areas correspond to the range of radii predicted for the estimated $T_{\rm eff}$ and age of the system by the Saumon & Marley (2008) models with cloudy (blue hatches), hybrid clouds (red hatches), and cloudless (green hatches; covering [M/H] of 0, 0.3, and –0.3 dex) atmospheres, considered as boundary conditions. The shaded zone correspond to the predictions of the COND models (Baraffe et al. 2003).

The BT-SETTL14 models do not provide any meaningful constraints on the log g. A reanalysis with a classical χ^2 confirms the conclusions. The radii (dilution factors) needed to adjust the surface flux, which were predicted by the models onto the apparent flux of the companion, are unphysical in the case of the BT-SETTL14 models. This may indicate that the $T_{\rm eff}$ of GJ 758 could be lower than the one corresponding to the best fit. The Exo-REM models fail to represent correctly the SED of the companion, especially in the Y-, H-, and K-bands.

We conclude that the companion has $T_{\rm eff}$ = 600 ± 100 K from the above analysis. This is in good agreement with Janson et al. (2011), whose analysis relied on the models of Burrows et al. (2006) but extended to colder temperatures (Hubeny & Burrows, in prep.). The Morley+12 parametric model points toward a low surface gravity, in agreement with the hints found in Sect. 5.2. But the non-existant exploration of the effect of the metal-enrichment in these grids of models, which are associated with model uncertainties, certainly biases the analysis. A low-resolution spectrum of the source is needed to determine log g and metallicity (M/H) with good confidence.

From the $T_{\rm eff}$ and the derived age for the system (3^{+3}_{-2} Gyr, see Sect. 4), we estimate a mass of 23^{+17}_{-13} $M_{\rm Jup}$ for GJ 758 B using the BT-SETTL13 grid of models (Allard et al. 2013). This value is in the low range of the masses inferred by Janson et al. (2011), as a direct consequence of our estimated age range for the system that is slightly younger than the one they considered.

Finally, we report in Table 9 the predictions from the Baraffe et al. (2003) and Saumon & Marley (2008) models. The models predict radii corresponding to the estimate $T_{\rm eff}$ in the range 0.80–1.21 $R_{\rm Jup}$, which are marginally consistent with the radii derived from the SED fit with the Exo-REM, Saumon12+, and Morley12+ models. They are still 25 and 11% larger than those infered from the SED fit with the BT-SETTL14-Y dwarfs and BT-SETTL14 models, respectively (see Fig. 7). The difference may arise from the different boundary conditions considered for the evolutionary models and the atmospheric models used for the SED fit. Nevertheless, it is more likely that the $T_{\rm eff}$ derived from the SED fit is slightly overestimated by the SETTL models (by 100–200 K) which leads to this inconsistency.

Table 9. $T_{\rm eff}$ and radius predictions from the Baraffe et al. (2003) and Saumon & Marley (2008) models.

Models	Boundary	M/H (dex)	R ($R_{\rm Jup}$)	Mass ($M_{\rm Jup}$)
Saumon+08	No cloud	0	$0.96^{0.14}_{0.10}$	24^{+16}_{-13}
Saumon+08	No cloud	+0.3	$0.97^{0.15}_{0.10}$	24^{+15}_{-14}
Saumon+08	No cloud	−0.3	$0.95^{0.15}_{0.10}$	24^{+16}_{-13}
Saumon+08	Cloudy	0.0	$1.01^{0.15}_{0.10}$	21^{+14}_{-11}
Saumon+08	Hybrid	0.0	$0.96^{0.13}_{0.10}$	24^{+14}_{-13}
COND	AMES-COND	0.0	$0.97^{0.05}_{0.08}$	21^{+11}_{-10}

5.4. Nature of the new candidate companion

The detection of a new candidate companion around a star with an already known companion is particularly interesting. It is going to become very common with the new generation of high-contrast imagers because of the boost in sensitivity that they provide at smaller angular separations. For the new candidate

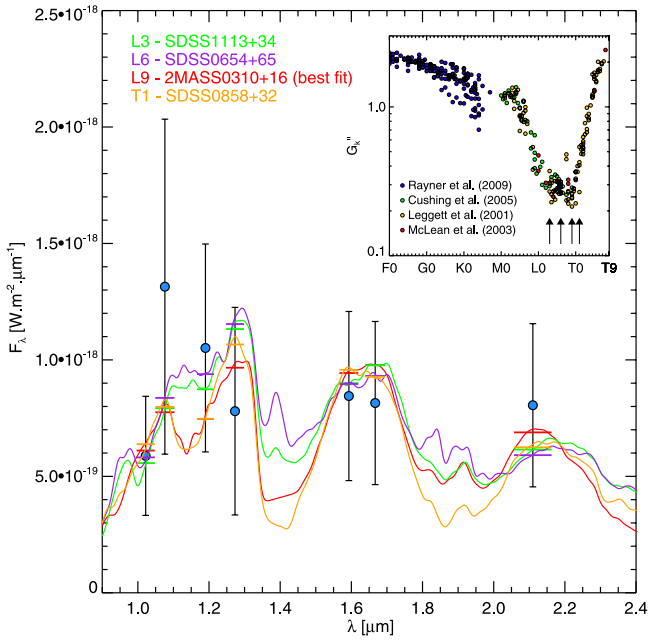

Fig. 8. Comparison of the flux of the newly identified candidate (blue circles) with SEDs of different substellar objects of spectral types L3, L6, L9 (best fit), and T1. For each spectral type, we plot the object that provides the best fit according to the G''_k indicator. The *inset plot* at the top shows the G''_k values as a function of spectral type for ∼400 objects taken from various libraries (Leggett et al. 2001; McLean et al. 2003; Cushing et al. 2005; Rayner et al. 2009). The vertical arrows indicate the spectral type of the plotted SEDs.

detected in our IRDIS data, we make use of the large multi-wavelength coverage (Y- to K-band) to perform a photometric analysis.

Although the error bars on the photometry of the new candidate are large (>0.5 mag, see Table 7), we attempt a first-order estimation of its spectral type by comparing its observed flux with the SEDs of stellar and substellar objects. The star data are taken from the IRTF stellar library[5] (Cushing et al. 2005; Rayner et al. 2009), while the brown dwarf data are taken from the NIRSPEC brown dwarf spectroscopic survey (McLean et al. 2003) and from Leggett et al. (2001). For the comparison, we use the G''_k indicator as in Sect. 5.2. The results are presented in Fig. 8, where we show the G''_k values as a function of spectral types (inset), and the SEDs of four objects that can equally well fit the photometry of the new candidate within the error bars.

The G''_k distribution shows a rather flat minimum in the L3–T1 range, indicating that our candidate could likely be of substellar nature. However, reaching a final conclusion is difficult from our current data because of the significant uncertainties on the photometry. As shown in Fig. 8, the candidate photometry is compatible with mid-L to early T-types, but late-M and early-L (not shown) would also provide decent fit. We note that the low galactic latitude of GJ 758 (+8 deg) significantly increases the probability of background contamination, particularly with late M stars, which are the main source of contamination at high-contrast (e.g., Chauvin et al. 2015).

Other possibilities for the nature of the candidate could include solar system bodies, such as asteroid and transneptunian objects, or extra-galactic objects. However, an asteroid basically reflects the near-IR light from the Sun, resulting in a very flat G2V spectrum that is not compatible with the photometry. In addition, these objects would be characterized by a very large proper motion of several mas to several dozens of mas per second. Our observations, taken over two consecutive nights, completely rule out this possibility. On the other hand, extragalactic sources such as galaxies are another possibility, but they would be resolved by the very fine plate scale of IRDIS (∼12.25 mas, see Table 3), even at significant redshifts. The point-like structure of the candidate also rules out this possibility.

In conclusion, we cannot rule out the possibility that the new companion is indeed bound to GJ 758 since its photometry is broadly compatible with L-type objects. A second epoch will be required to clear any possible doubt. Given the high proper motion of the star (∼180 mas/yr), a confirmation of the status of this candidate is already possible.

6. Astrometry and orbital properties

6.1. Least-Square Monte Carlo orbital fitting

We used the new IRDIS astrometric measurement to put constraints on the orbital solution of the system. In previous studies by Thalmann et al. (2009) and Janson et al. (2011), it was already shown that the system presents significant orbital motion and Monte Carlo simulations were used to get a first estimate of the orbital elements. In this study we first used a Least-Square Monte-Carlo (LSMC) approach to study the parameter space of possible orbits. For this purpose we created 5×10^6 sets of orbital elements, which were drawn from uniform distributions. These sets of orbital elements were then used as starting points for a least-squares minimization routine. The method is described in detail in Ginski et al. (2013). To limit the parameter space we fixed the total mass of the system to the nominal value of ∼1 $M_\odot$: 0.97 $M_\odot$ for the star (Takeda et al. 2007) and ∼0.03 $M_\odot$ for the companion at the probable age of the system. In addition, we limited the semi-major axis to values smaller than 63.45″ (1000 AU at a distance of 15.76 pc). This is assuming that the system is stable long-term against disruption in the galactic disk as described in Close et al. (2003). Given the high age of the system (3^{+3}_{-2} Gyr, see Sect. 4) and the fact that we still find the companion close to the host star, this assumption seems reasonable.

The results of our simulations are shown in Fig. 9. We do not show the results for the longitude of the ascending node and the argument of the periastron, since they are not well constrained yet by the available astrometry. In Fig. 10 we show the best fitting orbit solution that was recovered by the LSMC orbit fit. The corresponding orbital elements are shown in Table 10, alongside the results recovered from our Markov chain Monte Carlo (MCMC) simulation, which we discuss in the following section.

Since the orbit does not show significant curvature yet, we cannot put an upper limit on the semi-major axis or the eccentricity. However, we find a lower limit of 0.14 for the eccentricity and 21.9 AU (1.39″) for the semi-major axis. In general, the semi-major axis of possible orbits scales with the eccentricity, as can be seen in Fig. 9a. The minimum values of the semi-major axis and the eccentricity, as well as the general behavior of the well fitting orbit solutions, is consistent with the results presented in Janson et al. (2011), which were derived from simple Monte Carlo simulations.

In Fig. 9b we show the inclination of possible orbital solutions as a function of eccentricity. For close to face-on orbits (inclination close to 0 deg) we can constrain the eccentricity of the orbit to values between 0.47 and 0.55. This range grows

[5] http://irtfweb.ifa.hawaii.edu/~spex/IRTF_Spectral_Library/

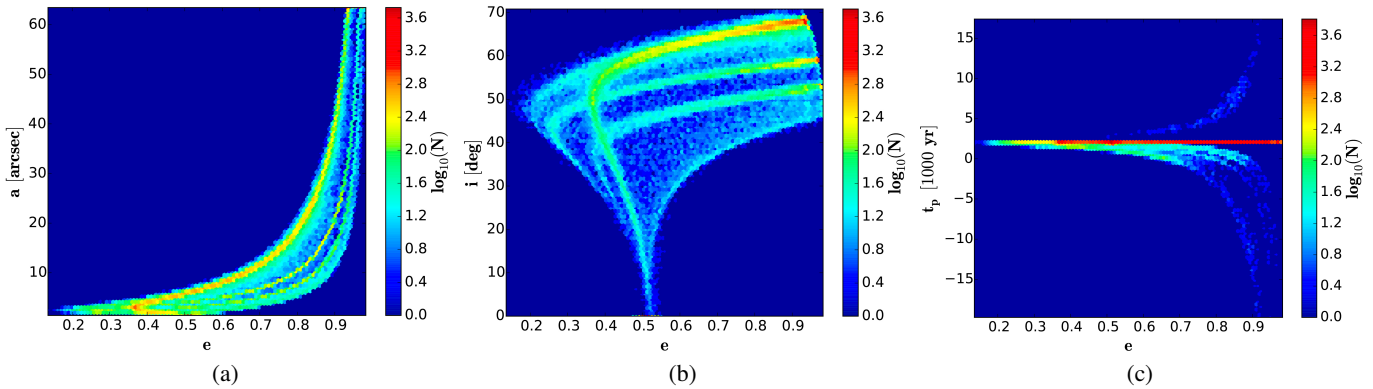

Fig. 9. Semi-major axis, inclination, and time of periastron passage as function of eccentricity for all solutions with $\chi^2_{\rm red} \leq 2$ out of 5 000 000 runs of our least-squares Monte Carlo (LSMC) fit. Logarithmic density of solutions is indicated by color.

continuously larger with increasing orbit inclination. For an inclination of ~50 deg, the full range of recovered eccentricities gives results that are consistent with the astrometric measurements. We can put an upper limit on the inclination of 70.8 deg, i.e., we can exclude edge-on orbit solutions. If we compute a simple median of the recovered orbit inclinations, we get a value of 58.9 ± 18.8 deg. This is, within the given uncertainties, consistent with the interval found in Janson et al. (2011). Inclinations smaller than 40 deg correspond to small semi-major axes, with an upper limit of 77.5 AU (4.92″) while, for larger values of the inclination, orbit solutions with the full range of recovered semi-major axes are possible.

Finally, in Fig. 9c we show the times of the periastron passage that we recovered from our simulations. The vast majority (87.5%) of our solutions pass the periastron between the years 2000 and 2065. The solutions that show the periastron passage at the time of the observations are generally highly eccentric and have large semi-major axes, which would explain that no curvature of the orbit has yet been observed.

While these solutions fit the orbit very well geometrically, they are, however, very unlikely, given that the companion would spend the vast majority of time at much larger separations from the primary star than where it was discovered. Indeed, if we use the orbital period of roughly 26 000 yr of the best-fitting LSMC orbit, we can estimate that the probability of finding the companion within 30 yr of the periastron passage is only approximately 0.1%. However, the orbits that pass the periastron within the next few decades could have lower eccentricities and semi-major axes. For an eccentricity of around ~0.5 there is a strong peak for the time of the periastron passage in the year 2040. It is thus of great interest to continue an astrometric monitoring of this system, since significant acceleration (i.e., curvature of the orbit) is to be expected, especially for cases with non-extreme eccentricities.

Since it will be very interesting if the system does indeed exhibit a high eccentricity (i.e., for the plausibility of scattering scenarios during its early formation), we examine how reliable the eccentricities of our recovered orbit solutions are. Pearce et al. (2014) study the possibility that an unknown inner (sub)stellar companion could introduce a false-positive eccentricity signal in the relative astrometry between the primary star and the known, directly imaged, companion. This is due to the astrometric displacement of the primary star as it orbits around the common center of mass with the hypothetical inner companion. We use their formalism to calculate the mass and angular distance that would be required for such an inner companion to make the orbit solution for GJ 758 B appear eccentric when, in fact, the real orbit is circular. We do this for all the orbit solutions that fit the astrometric measurements and the results are shown in Fig. 11. We find that a hypothetical inner companion would need a mass between 0.02 $M_\odot$ and 0.14 $M_\odot$ with an orbit separation of 0.42″ (6.6 AU; depending on the mass of the system and the epoch difference of the astrometric observations). For the large majority of our solutions, we can reject such a companion because it would have been discovered in our deep IRDIS images (see Sect. 7 for detection limit estimations). However, because of the old age of the system, we would not have been able to recover inner companions with masses below ~0.05 $M_\odot$ at the required angular separation.

To exclude the remaining possible solutions, we retrieved archival radial velocity data of GJ 758 A obtained with the ELODIE high-precision fiber-fed echelle spectrograph (Baranne et al. 1979), which coveris a time baseline of 7.8 yr, as well as archival data from the Lick Planet Search program, which covers 13.2 yr (Fischer et al. 2014). These combined data, shown in Fig. 12, covers a total of 16 yr. The data can be used to reject any hypothetical companion on a 17-yr period more massive than 0.02 $M_\odot$ that has any inclination greater than five degrees. Given the spherical symmetry of the system, this translates into a rejection of 98% of the orbital solutions for a hypothetical 0.02 $M_\odot$ inner companion and an increasing rejection rate for higher masses. It is thus extremely unlikely that the observed eccentricity is due to an inner companion causing an astrometric signal.

6.2. Markov chain Monte Carlo orbital fitting

The use of the MCMC technique to fit orbits of companions, either detected by radial velocity or by direct imaging, has become very popular in recent years. In relation to imaged planetary or substellar companions, it was for instance successfully applied to β Pictoris b (Chauvin et al. 2012; Nielsen et al. 2014; Macintosh et al. 2014), Fomalhaut b (Kalas et al. 2013; Beust et al. 2014), and to the four-planet system of HR 8799 (Pueyo et al. 2015).

MCMC is particularly well-suited for imaged companions for which the observational follow-up usually covers only a small part of the whole orbit (because of large orbital periods). To fit GJ 758 B's orbit, we first used the code already used to fit β Pictoris b's (Chauvin et al. 2012) and Fomalhaut b's (Beust et al. 2014) orbits. But, given the number of solutions at very

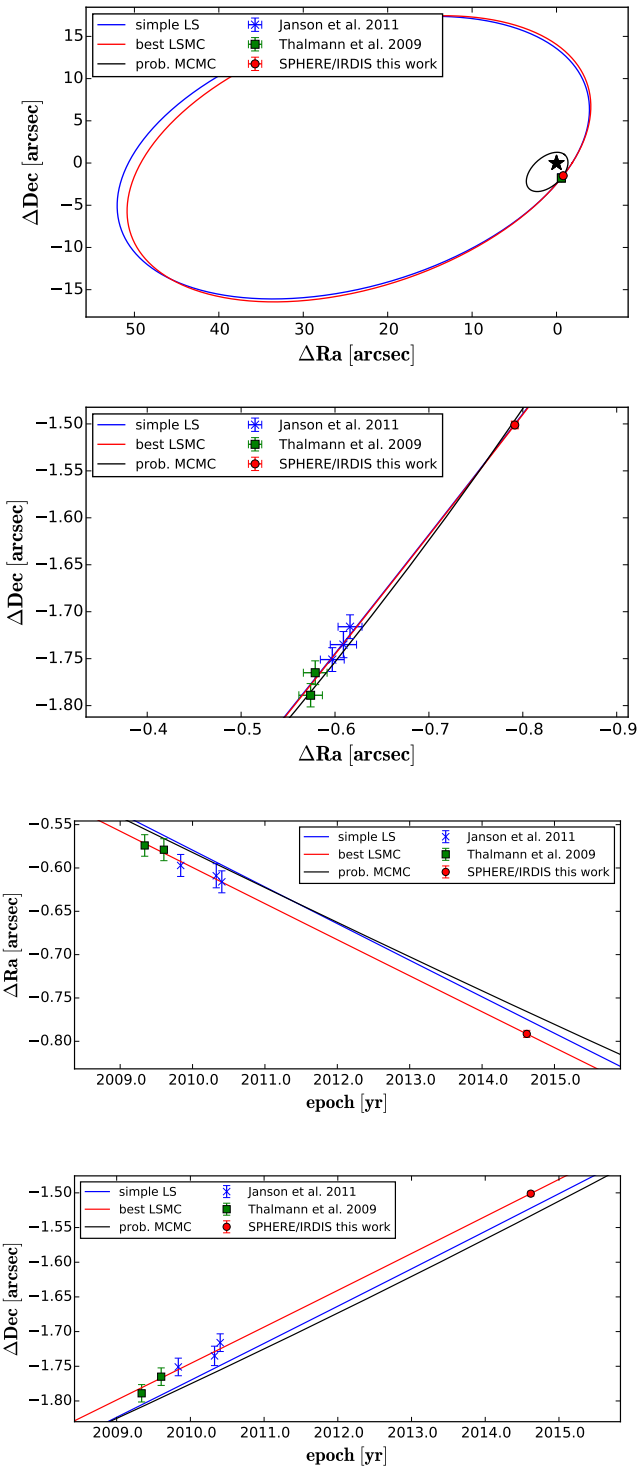

Fig. 10. Best-fitting orbits recovered with simple least squares fitting as well as LSMC fitting. In addition, we show a probable orbit with orbital elements close to the peak values, recovered by our MCMC fit (see Sect. 6.2). Solid lines represent the apparent orbits. The corresponding orbital elements are listed in Table 10. We show the data points taken with Subaru/HiCIAO (green squares) as given in Thalmann et al. (2009), as well as the data points taken with Subaru/HiCIAO, Gemini/NIRI and Keck/NIRC2 (blue crosses) given in Janson et al. (2011), together with our SPHERE/IRDIS measurement (red circle).

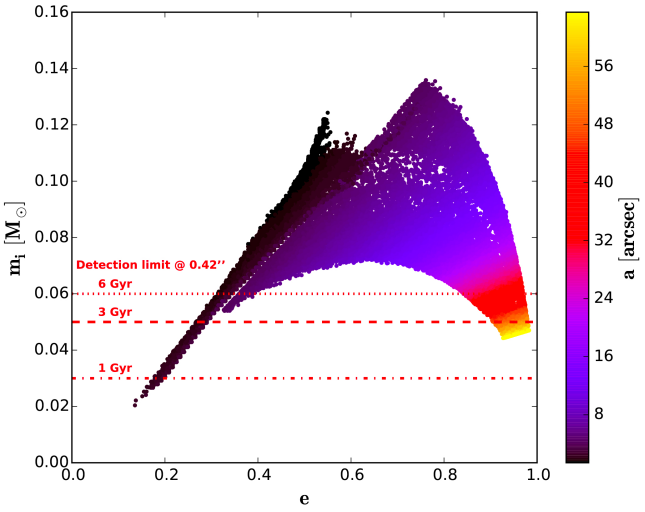

Fig. 11. Minimum mass of an unseen inner companion that would cause a false positive eccentricity signal in the relative astrometry of GJ 758 A and B by astrometric displacement of GJ 758 A due to their common orbit around the center of mass of the system. The minimum mass is a function of the eccentricity and semi-major axis of the A/B system as well as the maximum epoch difference of all astrometric measurements. Shown are such minimum masses for all orbits with $\chi^2_{\rm red} \leq 2$ which were recovered for the A/B system. Using our deep SPHERE/IRDIS observations as well as the AMES-COND models Baraffe et al. (2003) we also show the detectable minimum mass at the angular separation at which such a putative inner companion would need to reside. We can exclude the presence of an object that would introduce a false positive eccentricity in all cases.

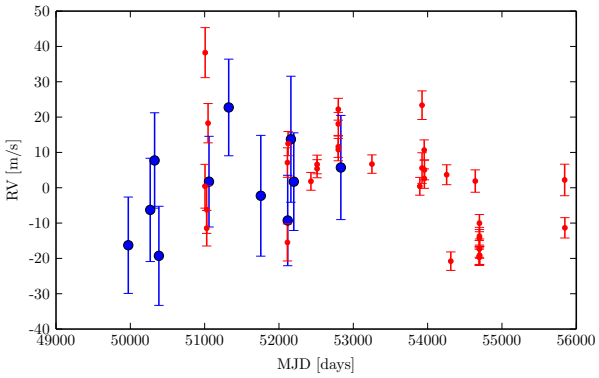

Fig. 12. Radial velocity (RV) measurements of GJ 758 A, retrieved from the ELODIE (large blue dots) and Lick Planet Search (small red dots) archives. The measurements cover a total of 16 yr, which is nearly the full period of the inner companion, as speculated from the astrometric signal.

large eccentricities that were hard to reach (the best-fit solution has eccentricity ~0.93; see Table 10), we moved to the use of another code that we have developed recently, which is based on the use of universal Keplerian variables with the Metropolis-Hastings algorithm and using Gibbs sampling as a convergence test. Universal variable formulation (Danby & Burkardt 1983; Burkardt & Danby 1983; Danby 1987) is an elegant way to provide a unique and continuous description of the Keplerian motion and is valid for any kind of orbit, whether bound or unbound. The details of this code will be presented in Beust et al. (in prep.). This code can handle both bound and unbound orbits, and is therefore not limited to elliptic orbits. It is thus well suited for very eccentric orbits.

Finding very eccentric orbital solutions should indeed not be surprising. As was shown by Pearce et al. (2015), whenever astrometric orbits are followed over small orbital arcs, more or

less arbitrarily eccentric solutions can be found depending on the unknown values of the z-coordinate and velocity along the line of sight. By and large, this situation applies here. At least from a mathemetical point of view, unbound solutions should be valid as well. This motivated us to use the universal variable code.

Ten chains were run in parallel until the Gelman-Rubin parameters $\hat{R}$ and $\hat{T}$ (Ford 2006) repeatedly reached convergence criteria for all parameters, i.e., $\hat{R} < 1.01$ and $\hat{T} > 1000$. This occurred after 5.2×10^8 steps. At this point, a sample of 10^6 orbital solutions is taken from the chains as representative for the posterior distribution of orbits. The orbital parameters considered are the periastron q, the eccentricity e, the inclination i with respect to the sky plane, the longitude of ascending node Ω (counted from north), the argument of periastron ω, and the time for periastron passage t_p. Here, we consider the periastron instead of the semi-major axis, as the periastron assumes a continuous distribution from elliptical to hyperbolic orbits. The priors on those elements are assumed as being uniform for Ω, ω, e, and t_p, logarithmic for q and $\propto \sin i$ for i. Combined with a uniform prior for Ω, the latter choice ensures a uniform probability distribution over the sphere for the direction of the orbital angular momentum vector. We emphasize that this choice of prior, especially concerning the eccentricity, is not dictated by physical likelihood considerations, but rather by mathematical constraints on the sole basis on the available astrometric data. While a linear eccentricity prior between 0 and 1 can be realistic, clearly unbound orbits appear unprobable, given the age of the star. The probability of witnessing an ejection or a flyby right now is indeed very low. But, as very eccentric solutions appeared to be compatible with the astrometric data, we wanted to allow the MCMC code to explore the unbound regime to estimate the actual constraints on the data and to avoid the introduction of artificial cut-offs.

The resulting posterior distribution is shown in Fig. 13, where probability histograms for individual elements are displayed as well as density maps for all possible pairs of parameters. The red bars that appear on the histogram plots, as well as the black stars in the bidimensional maps, correspond to the best χ^2 solution that was derived using a least-square Levenberg-Marquardt fitting scheme before launching MCMC. This solution has a reduced $\chi^2 = 0.419$, but more than 80% of the solutions in our posterior sample have reduced $\chi^2 < 1.5$. Peak values, confidence intervals, as well as details about the best χ^2 solution, are given in Table 10. Figure 13 shows that the eccentricity distributions extend beyond $e = 1$, so that we have both bound and unbound solutions in our sample. The upper limit at $e = 2$ in the eccentricity distribution is not physical. This threshold was fixed at the beginning of the simulation to save computing time.

The plots involving Ω and ω appear twofold, with similar patterns saparated by $\pm 180°$. This is a direct consequence of the degeneracy of the projected astrometric motion (Beust et al. 2014). To each solution with (Ω, ω) values, we find a corresponding twin solution with the same other orbital elements, but with $(\Omega + \pi, \omega + \pi)$. Both generate the same projected orbital motion.

Our initial comment on the result is that the orbit is clearly eccentric. However, despite the presence of unbound solutions in our sample, and although the best χ^2 solution appears very close to $e = 1$, most solutions have moderate eccentricities $\lesssim 0.7$, with a peak around $e = 0.5$. In our sample, 68% of orbits are bound. This is enough to confirm that GJ 758 B is very probably a bound companion to GJ 758, as an unbound orbit would mean an ongoing flyby or a very recent ejection. As both configurations can be regarded as improbable (though not impossible), finding more than two-thirds of bound solutions in our sample is a very strong indication of a bound orbit. If 68% can be taken as the minimum probability to have a bound orbit, then the actual probability is, in fact, much higher.

As noted above, this value is very probably far below the actual probability, since an unbound orbit would mean an ongoing flyby or a very recent ejection. This is a very improbable configuration given the age of the star. We regard 68% as the minimum probability to have a bound orbit without any physical consideration about the likelihood of unbound configurations. It is thus sufficiently high to allow us to claim that GJ 758 B is actually a bound companion to GJ 758 A. Based on the ratio between the timescale of an ejection event and the age of the star, the actual probability o observing one today should not exceed $\sim 10^{-6}$.

The periastron lies in the range 10–40 AU for about 70% of solutions, so that this must be regarded as the most probable range, with a clear probability peak at $q = 20$ AU. Indeed, solutions with higher q values correspond mostly to unbound solutions, and must therefore be considered as less probable.

All orbital solutions have inclination i well below 90°, compatible with a prograde motion as seen from the Earth. The inclination peaks around 60°, while the longitude of ascending node Ω exhibits a clear peak at $\sim -40°$. This shows that the orbital plane of GJ 758 B is rather well constrained. Conversely, the argument of periastron ω is very badly constrained. This is a direct consequence of the eccentricity dispersion of the solutions, as can be seen from the (ω, e) density maps (Fig. 13). The periastron passage is, however, better constrained with the next occurrence of a peak in 2039.

6.3. Conclusion on astrometry

To better compare LSMC and MCMC results, we created matching bidimensional density maps, which are restricted to bound orbits, and which consider the semi-major axis a and the eccentricity e, as well as the inclination i. For the MCMC results we restricted ourselves to bound solutions only. To match the MCMC results closely, we cut off the LSMC results at semi-major axes smaller than 10″. The results are shown in Fig. 14. We first show posterior MCMC distribution for the semi-major axis and the orbital period (left plots). Although both histograms exhibit tails towards large values (and thus approaching unbound orbits), we see that clear peaks appears around ~40 AU and ~200 yr. These values must be taken as the most probable ones. Then we compare the 2D maps that were generated by MCMC and LSMC (middle and right plots). An immediate comparison shows that both approaches agree very well and derive the same well-fitting range of bound orbital solutions. The differences in the density of solutions are likely caused by the difference of prior distributions that were used as input for both methods. While we considered uniform distributions in a and i for LSMC, we used distributions that were uniform in $\log q$ and $\propto \sin i$ for i. We did this because the aim of the methods is somewhat different. With LSMC, we aim to find the full possible range of geometrically well-fitting orbits, as well as the best-fitting orbit in terms of $\chi^2_{\rm red}$. With MCMC, on the other hand, the goal is to find the correct posterior probability distribution, given our prior knowledge of the system. This includes knowing that shorter period orbits are more likely given where we find the companion in our observation epochs, as well as the statistical likelihood of orbit inclinations.

We emphasise that the general results obtained by both methods agree very well. In particular, with LSMC we find an upper limit of the inclination of bound orbits of 70.8 deg, while the upper limit of the 1σ confidence interval recovered by LSMC

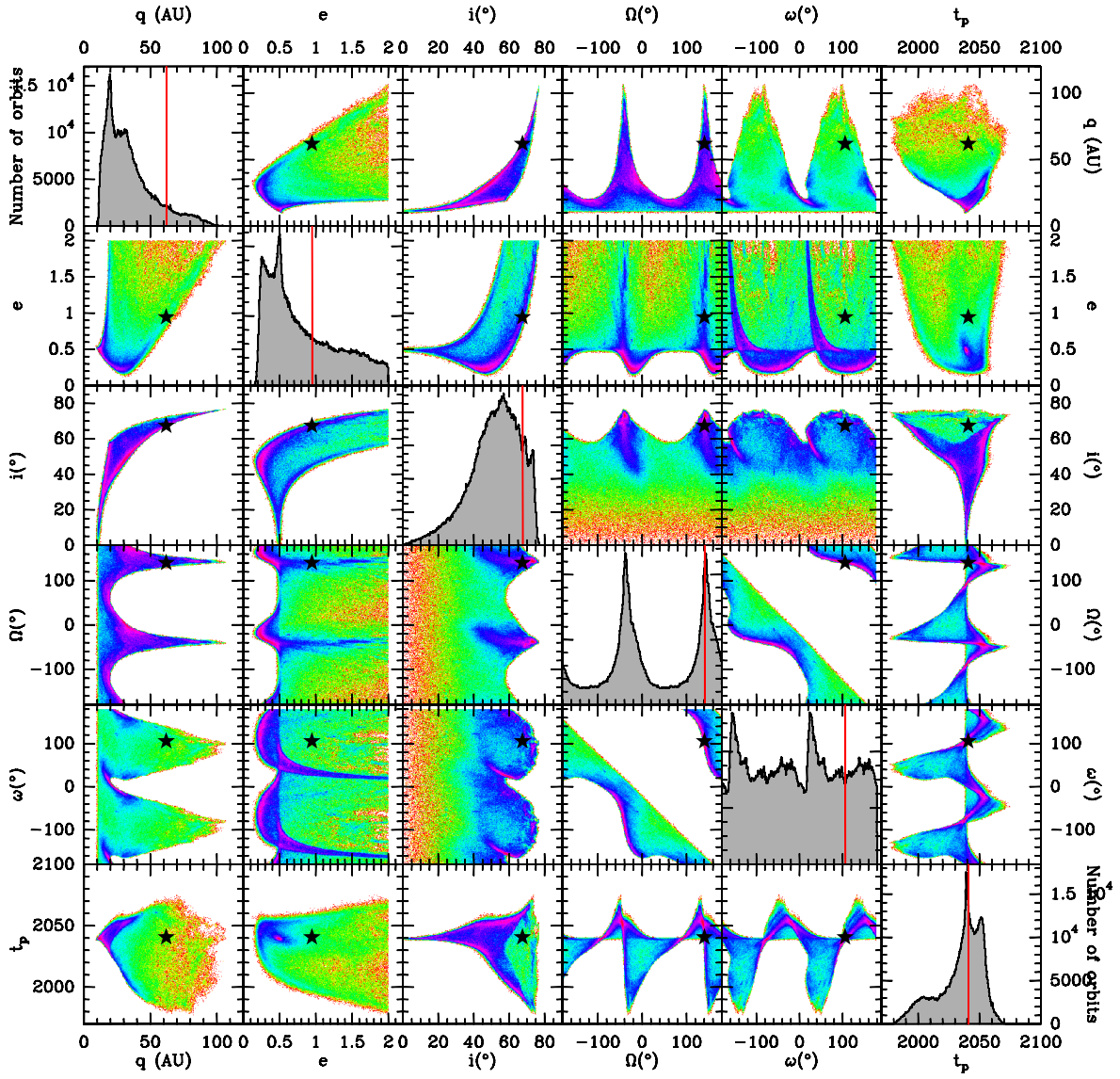

Fig. 13. Resulting MCMC posterior distribution of the six orbital elements (q, e, i, Ω, ω, t_p) of GJ 758 B's orbit using the universal variable code. The diagonal diagrams show mono-dimensional probability distributions of the individual elements. The off-diagonal plots show bidimensional probability maps for the various couples of parameters. This illustrates the correlation between orbital elements. The logarithmic color scale in these plots is linked to the relative local density of orbital solutions, as indicated to the side of Fig. 14. In the diagonal histograms, the red bar indicates the location of the best χ^2 solution, obtained via standard least-square fitting. The location of this solution is shown with black stars in the off-diagonal plots. This solution is also plotted in Fig 10.

is 70.3 deg. Both methods also find strong peaks in the time of the periastron passage between the years 2039 and 2040. Furthermore, the MCMC fit recovered 68% of bound orbit solutions. Given this high likelihood of a bound orbit and the high chance of a periastron passage within the next few decades, the GJ 758 system remains an interesting target for continued orbital monitoring. Orbit curvature will likely be discovered in this timeframe, allowing for a much better constrained determination of the companion's orbit.

7. Sensitivity to additional companions

To conclude our analysis, it is interesting to look at our sensitivity to additional massive companions in the GJ 758 system. We calculated detection limits in the different *DBI* filters following an ADI analysis with KLIP. The limits were estimated by measuring the standard deviation of the residuals in annuli of width 1 λ/D at increasing angular separation, divided by the maximum of the off-axis PSF of the star in the same filter. To properly take the effect of self-subtraction that was induced on the detection limits into account, the algorithm throughput was estimated by injecting fake companions, regularly spaced from 0.1″ to 2.0″, into the pre-processed data cubes. They were injected at a level ten times higher than the noise residuals in the final images at the separation of each of the companions. This process was repeated ten times with different orientations of the pattern of fake companions to average out possible variations of the throughput as a function of the position in the field. The throughput at each separation was then calculated to be the mean throughput over the ten measurements.

Taking into account the throughput in the different filters, the final detection limits are plotted in the right-hand panel of Fig. 15. Because of the small amount of field rotation in all observing sequences ($\lesssim 8^o$), the throughput of the analysis

Table 10. Orbital characteristics of the best χ^2 solution, recovered by simple least-squares fitting (*first column*) as well as LSMC fitting (*second column*) for GJ 758 B and statistical properties of the posterior distribution.

Parameter	Best simple χ^2 solution	Best LSMC solution	Probable MCMC solution	MCMC peak value	67% confidence interval	95% confidence interval
a (AU)	879.29	878.62	46.05	33.6	[19.7–83.7]	[19.7–348.7]
a (arcsec)	55.79	55.75	2.922	2.132	[1.250–5.311]	[1.250–22.126]
q (AU)	61.55	63.26	21.87	19.84	[9.99–38.11]	[9.99–74.75]
e	0.93	0.928	0.525	0.505	[0.205–0.993]	[0.133–1.78]
i(°)	67.37	68.08	46.05	56.63	[43.6–70.3]	[25.0–77.0]
Ω(°)	−38.81	−38.78	−49.93	-37.15 ± 180	...	...
ω(°)	−73.67	−73.98	4.90	-155.47 ± 180	...	...
t_p (yr AD)	2040.74	2040.98	2051.89	2039.3	[2015.4–2051.4]	[1993.8–2059.7]
P (yr)	26 073.26	26 046.36	312.48	128.3	[57.6–502.0]	[57.6–4287.0]
$\chi^2_{\rm red}$	0.419	0.417	1.434	...	...	...

Notes. In addition, we give an example for a probable orbit (orbital elements close to MCMC peak values) that was recovered by MCMC (*third column*). Note that Ω and ω are defined within a ±180° degeneracy, so that giving confidence intervals is meaningless. Peak and confidence intervals for a and P in the MCMC analysis are defined for bound orbits.

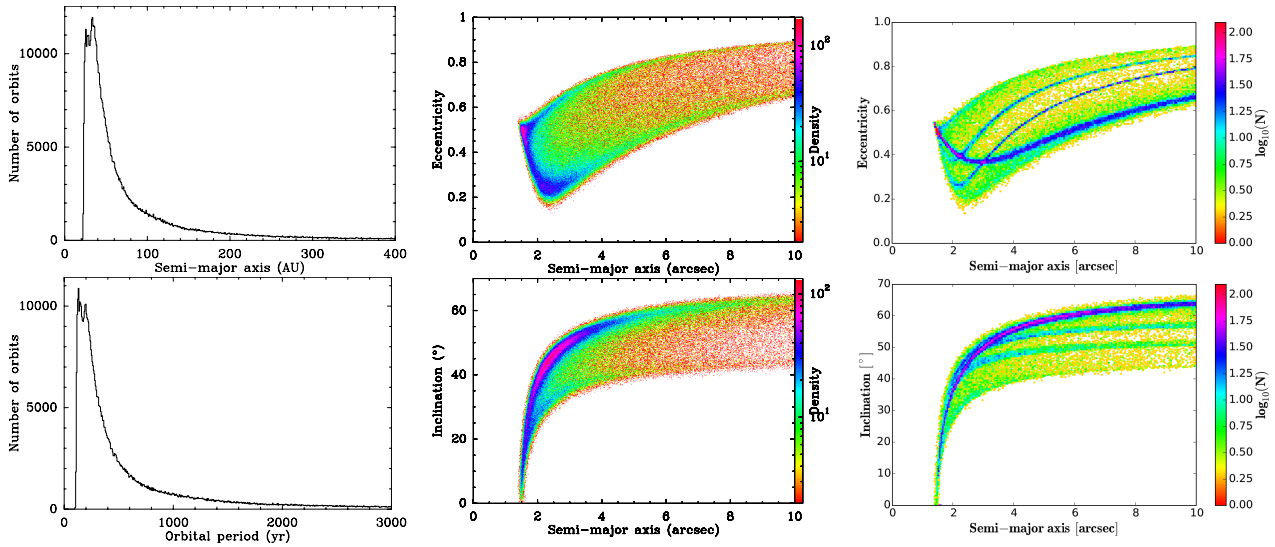

Fig. 14. *Left and middle*: additional plots to Fig. 13 restricted to bound orbits recovered only by our MCMC fit, showing i) posterior distributions of semi-major axis and orbital period (*left*); ii) bidimensional density maps, involving the semi-major axis a versus the eccentricity e and the inclination i. The color scale appearing to the right of the plots also applies to all similar plots in Fig. 13. *Right*: the same bidimensional density maps as shown in Fig. 14, showing orbit solutions recovered by our LSMC fit with semi-major axes smaller than 10″.

decreases significantly towards small angular separations, resulting in a sharp deterioration of the detection limits. It is only at separations larger than 0.21″, 0.25″, 0.33″, and 0.43″ that the field rotates by more than λ/D over the course of the complete sequence in Y-, J-, H-, and K-band respectively. The sensitivity is, nonetheless, improved compared with previous measurements below ∼0.5″.

The right-hand panel of Fig. 15 shows the conversion of these detection limits into physical units of projected separation and physical mass, using the known distance of the star (15.76 pc) and the AMES-COND evolutionary models (Baraffe et al. 2003) that were calculated in the IRDIS DBI filters. The two sets of curves represent the limit for the two extremes of the system's age range, 1–6 Gyr (see Sect. 4). For the youngest part of the age range, our observations clearly probe the low-mass brown-dwarf regime down to 4–5 AU, and even the planetary-mass regime beyond 20–30 AU. However, if we assume an older age for the system, i.e., more in line with the different age indicators, only massive brown dwarfs could be detected.

8. Summary and conclusions

Our new study of GJ 758 offers an improved overview of this interesting system. The brown-dwarf companion is redetected and we confirm some of its already known properties using our finer spectral sampling from SPHERE/IRDIS observations. In particular, we recover a low $T_{\rm eff} = 600 \pm 100$ K from a comparison of four different sets of models, which are in good agreement with previous studies (Thalmann et al. 2009; Currie et al. 2010; Janson et al. 2011). There are, however, some interesting peculiarities that are worth discussing.

In comparison to empirical objects, GJ 758 B appears as a very interesting object because we cannot find objects with known ages and metallicity to match all of its observed fluxes. We estimate a T8 spectral type for this object, but this estimation

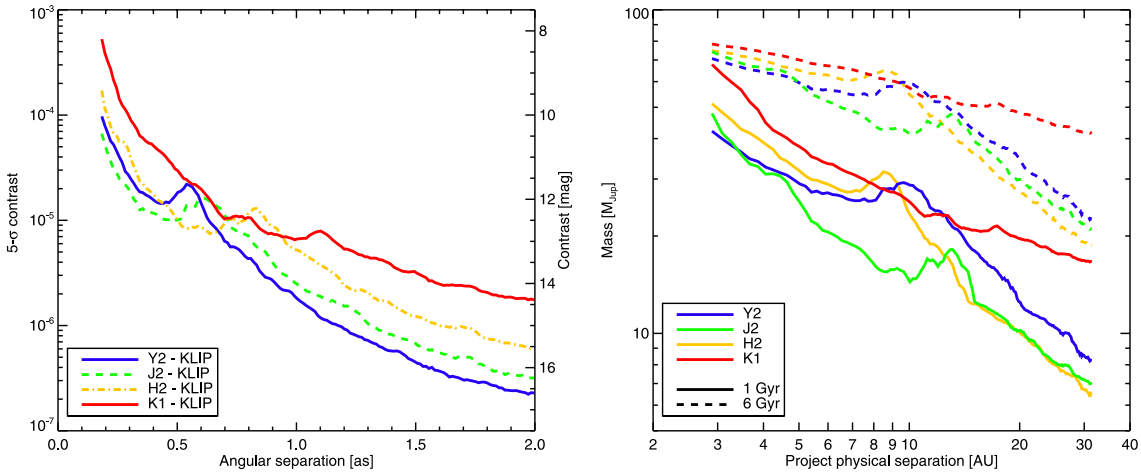

Fig. 15. *Left*: 5σ detection limits measured in the $Y2$, $J2$, $H2$, and $K1$ filters using a KLIP analysis, with a number of subtracted modes that vary to maximize the algorithm throughput. *Right*: conversion of these detection limits into physical units using the known distance of the GJ 758 system (15.76 pc) and the AMES-COND evolutinary tracks (Baraffe et al. 2003), calculated in the IRDIS filters. Two sets of curves assuming the two extremes of the system age range (1 and 6 Gyr, see Sect. 4) are displayed. The limits for the nominal age of 3 Gyr lie in-between, slightly closer to the 6 Gyr limit than the 1 Gyr limit.

is limited by the small amount of spectra of T8–T9 dwarfs with robust constraints on their ages and metallicity. One of the most likely explanations for the peculiar SED of this brown dwarf is the super-solar metallicity of the primary ([Fe/H] = 0.18 ± 0.05; see Sect. 4.2) and of the companion, if we assume they share the same metal enrichment. This is supported by the fact that the T8pec companion to the metal-poor dwarf BD+01 292 (Pinfield et al. 2012) shows a K-band spectral deviation opposite to that of GJ 758 B. Unfortunately, the current lack of such companions precludes us from performing a meaningful comparison. Similarly, a comparison with synthetic grids of models is constrained by the limited extension of most grids toward non-solar metallicities and low $T_{\rm eff}$ values. None of the four types of models that we tested was able to accurately reproduce the photometry of GJ 758 B in all filters. The J3 and H2 fluxes are especially difficult to reproduce and cannot be readily explained with any of the models. The BT-SETTL14 models (Allard et al. 2013), with an enrichment of 0.3 dex in α elements with respect to solar composition, do provide a better fit of the J3 flux, but at the expense of much smaller dilution factors, which correspond to unphysical values of the companion radius (∼0.7 $R_{\rm Jup}$). Even so, the high H2 flux is not reproduced. This could actually indicate that the $T_{\rm eff}$ of GJ 758 B might be even lower than the one of the best fit but we are limited by the absence of metal-enriched models at very low $T_{\rm eff}$. As a result, our analysis confirms the low $T_{\rm eff}$ of the object, corresponding to a mass of 23^{+17}_{-13} $M_{\rm Jup}$ in the considered age range (using the Baraffe et al. 2003 evolutionary tracks), but we cannot infer any precise value for $\log g$ and M/H. The study of this object would strongly benefit from low-resolution spectroscopy, e.g., with IRDIS long-slit spectroscopy mode (Vigan et al. 2008).

The new astrometry confirms the picture of a very eccentric companion. As reported by Janson et al. (2011), the curvature of the orbit is still not detectable yet. The ∼0.28″ motion of the companion along its orbit roughly appears as a straight line from the previous measurements taken in 2010. Our LSMC and MCMC simulations favour an eccentric – but bound – orbit, with a high likelihood of $e \simeq 0.5$. In particular, no orbital solution shows an eccentricity lower than 0.14, which is consistent with previously reported results and is between our two approaches ([0.133–1.78] 95% confidence interval from MCMC). In addition, we have ruled out the possibility that the observed eccentricity is just caused by a massive closer-in companion that would create a false positive eccentricity by astrometric displacement of the primary. Indeed, although not extremely accurate, our radial velocity (RV) data reject a companion that is more massive then 0.02 $M_{\odot}$ on periods shorter than 17 yr and an inclination that is larger than 5 deg. Finally, our new IRDIS observations reject the possibility of an additional companion that is more massive than ∼30–40 $M_{\rm Jup}$ (for ages of 1–3 Gyr) above 4–5 AU.

In the light of our constraints on the orbit and mass of GJ 758 B, it is interesting to look into the formation of this object. While our study does not bring enough new material in favor or against planet-like formation scenarios (core accretion vs. gravitational instability, migration, etc.), we can instead focus on stellar-like formation scenarios. Several past studies have argued for a universal companion mass function (CMF) for stellar and substellar companions. In particular, in their in-depth anaysis focused on brown dwarfs around solar-type stars, Metchev & Hillenbrand (2009) find tentative evidence for such a universal CMF and predict a peak in semi-major axes for brown dwarfs at ∼30 AU. From this point of view, it makes sense to compare the properties of the GJ 758 system to the properties of solar-type multiple systems. (Raghavan et al. 2010) have published the most complete study on this topic to date. While we cannot compare quantitatively our results on a single object with their global multiplicity analysis, it is interesting to note a few qualitative facts. Firstly, with a most likely period of 312.48 yr (from MCMC, see Table 10), GJ 758 B falls exactly at the peak of their period distribution (293.57 yr; Raghavan et al. 2010, Fig. 13). Secondly, with a most likely eccentricity of 0.525, GJ 758 B falls in the bulk of their eccentricity-period distributions. And thirdly, with a ratio $q = M_2/M_1 = 0.023 \pm 0.013$, the GJ 758 systems falls at the very edge of the study of Raghavan et al. (2010), but in their q-period plot, the system is not completely isolated and could be part of the tail of the distribution. While these facts do not prove that the system was formed in a stellar way, they certainly support this possibility qualitatively.

In conclusion, GJ 758 B remains a very interesting object that warrants i) deeper observations to look for additional companions in the system; ii) spectroscopic observations

to better constrain its physical properties, and iii) astrometric monitoring to get tighter constraints on its eccentric orbit.

Acknowledgements. A.V., M.B., G.C., G.S., J.-L.B., and D.M. acknowledge support in France from the French National Research Agency (ANR) through project grant ANR10-BLANC0504-01, the CNRS-D2P PICS grant, and the Programmes Nationaux de Planétologie et de Physique Stellaire (PNP & PNPS). J.-L.Ba.'s Ph.D is funded by the LabEx Exploration Spatiale des Environnements Planétaires (ESEP) #2011-LABX-030. V.D. is partially supported by the Australian Research Council. V.D., S.D., A.L.M., R.G., and D.M. acknowledge support from the Progetti Premiali funding scheme of the Italian Ministry of Education, University, and Research. E.B. and J.H. are supported by the Swiss National Science Foundation (SNSF). A.Z. acknowledges support from the Millennium Science Initiative (Chilean Ministry of Economy), through grant Nucleus RC130007. The authors warmly thank A. Bellini and J. Anderson for kindly providing the catalog positions of the stars in the 47 Tuc field before their publication. We are very grateful to D. Kirkpatrick, A. Burgasser, D. Pinfield, B. Burningham, and G. Mace for sending us the spectra of benchmark T–Y objects. We thank C. Morley, D. Saumon, and F. Allard for free online access to their atmospheric model grids, and F. Bouchy for his help with the ELODIE data. This research has benefitted from the SpeX Prism Spectral Libraries, maintained by Adam Burgasser at `http://pono.ucsd.edu/~adam/browndwarfs/spexprism`. This research has made use of the SIMBAD database, operated at CDS, Strasbourg, France. SPHERE is an instrument designed and built by a consortium consisting of IPAG (Grenoble, France), MPIA (Heidelberg, Germany), LAM (Marseille, France), LESIA (Paris, France), Laboratoire Lagrange (Nice, France), INAF – Osservatorio di Padova (Italy), Observatoire de Genève (Switzerland), ETH Zurich (Switzerland), NOVA (Netherlands), ONERA (France) and ASTRON (Netherlands), in collaboration with ESO. SPHERE was funded by ESO, with additional contributions from CNRS (France), MPIA (Germany), INAF (Italy), FINES (Switzerland), and NOVA (Netherlands). SPHERE also received funding from the European Commission Sixth and Seventh Framework Programmes as part of the Optical Infrared Coordination Network for Astronomy (OPTICON) under grant number RII3-Ct-2004-001566 for FP6 (2004–2008), grant number 226604 for FP7 (2009–2012), and grant number 312430 for FP7 (2013–2016).

References

Abel, M., Frommhold, L., Li, X., & Hunt, K. L. C. 2012, in APS Meet. Abstr., 26001
Ackerman, A. S., & Marley, M. S. 2001, ApJ, 556, 872
Allard, F., Hauschildt, P. H., Miller, S., & Tennyson, J. 1994, ApJ, 426, L39
Allard, F., Homeier, D., Freytag, B., et al. 2013, Mem. Soc. Astron. It. Suppl., 24, 128
Baraffe, I., Chabrier, G., Barman, T. S., Allard, F., & Hauschildt, P. H. 2003, A&A, 402, 701
Baranne, A., Mayor, M., & Poncet, J. L. 1979, Vistas Astron., 23, 279
Baudino, J.L., Bézard, B., Boccaletti, A., et al. 2015, A&A, 582, A14
Bellini, A., Anderson, J., van der Marel, R. P., et al. 2014, ApJ, 797, 115
Beust, H., Augereau, J.-C., Bonsor, A., et al. 2014, A&A, 561, A43
Beuzit, J.-L., Feldt, M., Dohlen, K., et al. 2008, in SPIE Conf. Ser., 7014, 18
Boccaletti, A., Abe, L., Baudrand, J., et al. 2008, in SPIE Conf. Ser., 7015, 1
Bohlin, R. C. 2007, in The Future of Photometric, Spectrophotometric and Polarimetric Standardization, ed. C. Sterken, ASP Conf. Ser., 364, 315
Borysow, A., Jorgensen, U. G., & Zheng, C. 1997, A&A, 324, 185
Bowler, B. P., Liu, M. C., Dupuy, T. J., & Cushing, M. C. 2010, ApJ, 723, 850
Bressan, A., Marigo, P., Girardi, L., et al. 2012, MNRAS, 427, 127
Brott, I., & Hauschildt, P. H. 2005, in The Three-Dimensional Universe with Gaia, eds. C. Turon, K. S. O'Flaherty, & M. A. C. Perryman, ESA SP, 576, 565
Buenzli, E., Apai, D., Morley, C. V., et al. 2012, ApJ, 760, L31
Burgasser, A. J. 2014, in AS India Conf. Ser., 11, 16
Burgasser, A. J., McElwain, M. W., Kirkpatrick, J. D., et al. 2004, AJ, 127, 2856
Burgasser, A. J., Simcoe, R. A., Bochanski, J. J., et al. 2010, ApJ, 725, 1405
Burgasser, A. J., Cushing, M. C., Kirkpatrick, J. D., et al. 2011, ApJ, 735, 116
Burningham, B., Leggett, S. K., Homeier, D., et al. 2011, MNRAS, 414, 3590
Burkardt, T. M., & Danby, J. M. A. 1983, Celes. Mech., 31, 317
Burningham, B., Pinfield, D. J., Leggett, S. K., et al. 2009, MNRAS, 395, 1237
Burrows, A., Sudarsky, D., & Hubeny, I. 2006, ApJ, 640, 1063
Caffau, E., Ludwig, H.-G., Steffen, M., Freytag, B., & Bonifacio, P. 2011, Sol. Phys., 268, 255
Chauvin, G., Lagrange, A.-M., Beust, H., et al. 2012, A&A, 542, A41
Chauvin, G., Vigan, A., Bonnefoy, M., et al. 2015, A&A, 573, A127
Close, L. M., Siegler, N., Freed, M., & Biller, B. 2003, ApJ, 587, 407
Currie, T., Bailey, V., Fabrycky, D., et al. 2010, ApJ, 721, L177
Cushing, M. C., Rayner, J. T., & Vacca, W. D. 2005, ApJ, 623, 1115
Cushing, M. C., Marley, M. S., Saumon, D., et al. 2008, ApJ, 678, 1372
Cutri, R. M., Skrutskie, M. F., van Dyk, S., et al. 2003, 2MASS All Sky Catalog of point sources
Cutri, R. M., et al. 2013, VizieR Online Data Catalog: II/328
da Silva, L., Girardi, L., Pasquini, L., et al. 2006, A&A, 458, 609
Danby, J. M. A. 1987, Celes. Mech., 40, 303
Danby, J. M. A., & Burkardt, T. M. 1983, Celes. Mech., 31, 95
De Silva, G. M., D'Orazi, V., Melo, C., et al. 2013, MNRAS, 431, 1005
Desidera, S., Covino, E., Messina, S., et al. 2011, A&A, 529, A54
Desidera, S., Covino, E., Messina, S., et al. 2015, A&A, 573, A126
Dohlen, K., Langlois, M., Saisse, M., et al. 2008, in SPIE Conf. Ser., 7014, 3
D'Orazi, V., & Randich, S. 2009, A&A, 501, 553
D'Orazi, V., Magrini, L., Randich, S., et al. 2009, ApJ, 693, L31
D'Orazi, V., Biazzo, K., Desidera, S., et al. 2012, MNRAS, 423, 2789
Duncan, D. K., Vaughan, A. H., Wilson, O. C., et al. 1991, ApJS, 76, 383
Dupuy, T. J., & Kraus, A. L. 2013, Science, 341, 1492
Faherty, J. K., Burgasser, A. J., Walter, F. M., et al. 2012, ApJ, 752, 56
Fischer, D. A., Marcy, G. W., & Spronck, J. F. P. 2014, ApJS, 210, 5
Ford, E. B. 2006, ApJ, 642, 505
Fusco, T., Rousset, G., Sauvage, J.-F., et al. 2006, Opt. Exp., 14, 7515
Fusco, T., Sauvage, J.-F., Petit, C., et al. 2014, in SPIE Conf. Ser., 9148, 15
Gagné, J., Lafrenière, D., Doyon, R., Malo, L., & Artigau, É. 2014, ApJ, 783, 121
Galicher, R., & Marois, C. 2011, in Second International Conference on Adaptive Optics for Extremely Large Telescopes, 25P, Online at `http://ao4elt2.lesia.obspm.fr`
Geballe, T. R., Kulkarni, S. R., Woodward, C. E., & Sloan, G. C. 1996, ApJ, 467, L101
Geballe, T. R., Saumon, D., Leggett, S. K., et al. 2001, ApJ, 556, 373
Ginski, C., Neuhäuser, R., Mugrauer, M., Schmidt, T. O. B., & Adam, C. 2013, MNRAS, 434, 671
Goldman, B., Marsat, S., Henning, T., Clemens, C., & Greiner, J. 2010, MNRAS, 405, 1140
Hauschildt, P. H., Baron, E., & Allard, F. 1997, ApJ, 483, 390
Hoeg, E., Bässgen, G., Bastian, U., et al. 1997, A&A, 323, L57
Hugot, E., Ferrari, M., El Hadi, K., et al. 2012, A&A, 538, A139
Isaacson, H., & Fischer, D. 2010, ApJ, 725, 875
Jacobson, H. R., & Friel, E. D. 2013, AJ, 145, 107
Janson, M., Carson, J., Thalmann, C., et al. 2011, ApJ, 728, 85
Jarrett, T. H., Cohen, M., Masci, F., et al. 2011, ApJ, 735, 112
Jones, A., Noll, S., Kausch, W., Szyszka, C., & Kimeswenger, S. 2013, A&A, 560, A91
Kalas, P., Graham, J. R., Fitzgerald, M. P., & Clampin, M. 2013, ApJ, 775, 56
Kovtyukh, V. V., Soubiran, C., & Belik, S. I. 2004, A&A, 427, 933
Kurucz, R. 1993, ATLAS9 Stellar Atmosphere Programs and 2 km s^{-1} grid. CD-ROM No. 13 (Cambridge, MA: Smithsonian Astrophysical Observatory)
Leggett, S. K., Allard, F., Geballe, T. R., Hauschildt, P. H., & Schweitzer, A. 2001, ApJ, 548, 908
Leggett, S. K., Burningham, B., Saumon, D., et al. 2010, ApJ, 710, 1627
Lucas, P. W., Tinney, C. G., Burningham, B., et al. 2010, MNRAS, 408, L56
Mace, G. N., Kirkpatrick, J. D., Cushing, M. C., et al. 2013, ApJ, 777, 36
Macintosh, B., Graham, J. R., Ingraham, P., et al. 2014, PNAS, 111, 12661
Maiorca, E., Magrini, L., Busso, M., et al. 2012, ApJ, 747, 53
Maire, A.-L., Boccaletti, A., Rameau, J., et al. 2014, A&A, 566, A126
Maire, A.-L., Bonnefoy, M., Ginski, C., et al. 2016, A&A, 587, A56
Maldonado, J., Eiroa, C., Villaver, E., Montesinos, B., & Mora, A. 2012, A&A, 541, A40
Malo, L., Doyon, R., Lafrenière, D., et al. 2013, ApJ, 762, 88
Mamajek, E. E., & Hillenbrand, L. A. 2008, ApJ, 687, 1264
Markwardt, C. B. 2009, in Astronomical Data Analysis Software and Systems XVIII, eds. D. A. Bohlender, D. Durand, & P. Dowler, ASP Conf. Ser., 411, 251
Marois, C., Lafrenière, D., Doyon, R., Macintosh, B., & Nadeau, D. 2006, ApJ, 641, 556
Marois, C., Macintosh, B., & Véran, J.-P. 2010, in SPIE Conf. Ser., 7736
Marois, C., Correia, C., Véran, J.-P., & Currie, T. 2014, in IAU Symp. 299, eds. M. Booth, B. C. Matthews, & J. R. Graham, 48
McLean, I. S., McGovern, M. R., Burgasser, A. J., et al. 2003, ApJ, 596, 561
Metchev, S. A., & Hillenbrand, L. A. 2009, ApJS, 181, 62
Mishenina, T., Korotin, S., Carraro, G., Kovtyukh, V. V., & Yegorova, I. A. 2013, MNRAS, 433, 1436
Monet, D. G., Levine, S. E., Canzian, B., et al. 2003, AJ, 125, 984
Morley, C. V., Fortney, J. J., Marley, M. S., et al. 2012, ApJ, 756, 172
Moultaka, J., Ilovaisky, S. A., Prugniel, P., & Soubiran, C. 2004, PASP, 116, 693
Neves, V., Bonfils, X., Santos, N. C., et al. 2014, A&A, 568, A121
Nidever, D. L., Marcy, G. W., Butler, R. P., Fischer, D. A., & Vogt, S. S. 2002, ApJS, 141, 503

Nielsen, E. L., Liu, M. C., Wahhaj, Z., et al. 2014, ApJ, 794, 158
Noll, S., Kausch, W., Barden, M., et al. 2012, A&A, 543, A92
Pavlov, A., Möller-Nilsson, O., Feldt, M., et al. 2008, in SPIE Conf. Ser., 7019, 39
Pearce, T. D., Wyatt, M. C., & Kennedy, G. M. 2014, MNRAS, 437, 2686
Pearce, T. D., Wyatt, M. C., & Kennedy, G. M. 2015, MNRAS, 448, 3679
Petit, C., Sauvage, J.-F., Fusco, T., et al. 2014, in SPIE Conf. Ser., 9148, 0
Pinfield, D. J., Burningham, B., Lodieu, N., et al. 2012, MNRAS, 422, 1922
Pueyo, L., Soummer, R., Hoffmann, J., et al. 2015, ApJ, 803, 31
Racine, R., Walker, G. A. H., Nadeau, D., Doyon, R., & Marois, C. 1999, PASP, 111, 587
Raghavan, D., McAlister, H. A., Henry, T. J., et al. 2010, ApJS, 190, 1
Rayner, J. T., Cushing, M. C., & Vacca, W. D. 2009, ApJS, 185, 289
Saumon, D., & Marley, M. S. 2008, ApJ, 689, 1327
Saumon, D., Bergeron, P., Lunine, J. I., Hubbard, W. B., & Burrows, A. 1994, ApJ, 424, 333
Saumon, D., Marley, M. S., Abel, M., Frommhold, L., & Freedman, R. S. 2012, ApJ, 750, 74
Sauvage, J.-F., Fusco, T., Petit, C., et al. 2014, in SPIE Conf. Ser., 9148
Scholz, R.-D. 2010, A&A, 515, A92
Sneden, C. A. 1973, Ph.D. Thesis, The university of Texas at Austin, TX (USA)
Soubiran, C., Bienaymé, O., Mishenina, T. V., & Kovtyukh, V. V. 2008, A&A, 480, 91
Soummer, R. 2005, ApJ, 618, L161
Soummer, R., Pueyo, L., & Larkin, J. 2012, ApJ, 755, L28
Takeda, Y. 2007, PASJ, 59, 335
Takeda, Y., & Kawanomoto, S. 2005, PASJ, 57, 45
Takeda, G., Ford, E. B., Sills, A., et al. 2007, ApJS, 168, 297
Thalmann, C., Carson, J., Janson, M., et al. 2009, ApJ, 707, L123
van Leeuwen, F. 2007, A&A, 474, 653
Vigan, A., Langlois, M., Moutou, C., & Dohlen, K. 2008, A&A, 489, 1345
Vigan, A., Moutou, C., Langlois, M., et al. 2010, MNRAS, 407, 71
Vigan, A., Patience, J., Marois, C., et al. 2012, A&A, 544, A9
Voges, W., Aschenbach, B., Boller, T., et al. 1999, A&A, 349, 389
Voges, W., Aschenbach, B., Boller, T., et al. 2000, IAU Circ., 7432, 1
Wright, J. T., Marcy, G. W., Butler, R. P., & Vogt, S. S. 2004, ApJS, 152, 261
Yong, D., Carney, B. W., & Friel, E. D. 2012, AJ, 144, 95

[1] Aix Marseille Université, CNRS, LAM (Laboratoire d'Astrophysique de Marseille) UMR 7326, 13388 Marseille, France
e-mail: arthur.vigan@lam.fr
[2] European Southern Observatory, Alonso de Cordova 3107, Vitacura, Santiago, Chile
[3] Université Grenoble Alpes, IPAG, 38000 Grenoble, France
[4] CNRS, IPAG, 38000 Grenoble, France
[5] Leiden Observatory, Leiden University, PO Box 9513, 2300 RA Leiden, The Netherlands
[6] LESIA, Observatoire de Paris, CNRS, Université Paris Diderot, Université Pierre et Marie Curie, 5 place Jules Janssen, 92190 Meudon, France
[7] Stockholm University, AlbaNova University Center, 10691 Stockholm, Sweden
[8] Max Planck Institute for Astronomy, Königstuhl 17, 69117 Heidelberg, Germany
[9] Institute for Astronomy, University of Hawaii, 2680 Woodlawn Drive, Honolulu, HI 96822, USA
[10] Geneva Observatory, University of Geneva, Chemin des Maillettes 51, 1290 Versoix, Switzerland
[11] INAF–Osservatorio Astronomico di Padova, Vicolo dell'Osservatorio 5, 35122 Padova, Italy
[12] Dept. of Physics and Astronomy, Macquarie University, NSW 2109, Sydney, Australia
[13] Monash Centre for Astrophysics, Monash University, VIC 3800, Melbourne, Australia
[14] ONERA, The French Aerospace Lab BP72, 29 avenue de la Division Leclerc, 92322 Châtillon Cedex, France
[15] Institute for Astronomy, ETH Zurich, Wolfgang-Pauli-Strasse 27, 8093 Zurich, Switzerland
[16] CNRS, CFHT, 65-1238 Mamalahoa Hwy, Kamuela HI, USA
[17] Núcleo de Astronomía, Facultad de Ingeniería, Universidad Diego Portales, Av. Ejercito 441, Santiago, Chile
[18] Millennium Nucleus "Protoplanetary Disk", Departamento de Astronomía, Universidad de Chile, Casilla 36-D, Santiago, Chile
[19] INAF–Osservatorio Astrofisico di Arcetri, Largo E. Fermi 5, 50125 Firenze, Italy
[20] University of Amsterdam Sterrenkundig Instituut "Anton Pannekoek" Science Park 9041098 XH Amsterdam, The Netherlands
[21] European Southern Observatory, Karl-Schwarzschild-Str. 2, 85748 Garching, Germany
[22] CRAL, UMR 5574, CNRS, Université Lyon 1, 9 avenue Charles André, 69561 Saint-Genis-Laval Cedex, France
[23] Université Nice-Sophia Antipolis, CNRS, Observatoire de la Côte d'Azur, Laboratoire J.-L. Lagrange, CS 34229, 06304 Nice Cedex 4, France
[24] California Institute of Technology, 1200 E. California Blvd, Pasadena, CA 91125, USA
[25] NOVA Optical-Infrared Instrumentation Group at ASTRON, Oude Hoogeveensedijk 4, 7991 PD Dwingeloo, The Netherlands

Appendix A: Description of the atmospheric models

Table A.1. Characteristics of the atmospheric model grids adjusted on the SED of GJ 758 B.

Model name	$T_{\rm eff}$ (K)	$\Delta T_{\rm eff}$ (K)	$\log g$ (dex)	$\Delta\log g$ (dex)	[M/H] (dex)	[α] (dex)	$f_{\rm SED}$
BT-SETTL14-Y	200–420	20	3.5–4.5	0.5	0.0	0.0	n/a
BT-SETTL14-Y	450–1000	50	3.5–4.5	0.5	0.0	0.0	n/a
BT-SETTL14	500–3000	50	3.5–5.5	0.5	0.0	0.0	n/a
BT-SETTL14	500–2800	100	4.0–5.5	0.5	0.0	0.3	n/a
Exo-REM - NC	400–1300	100	3.5–5.5	0.2	–0.5,0,+0.5	0.0	n/a
Exo-REM - T3	400–1300	100	3.5–5.5	0.2	–0.5,0,+0.5	0.0	n/a
Morley+12	400–600	50	4.0–5.5	0.5	0.0	0.0	2, 3, 4, 5
Morley+12	600–1200	100	4.0–5.5	0.5	0.0	0.0	2, 3, 4, 5
Saumon+12	300–350	50	3.75,4.0–5.0	0.25,0.5	0.0	0.0	∞
Saumon+12	300–1200	50	3.0–4.75,5.0-5.5	0.25,0.5	0.0	0.0	∞
Saumon+12	1300–1500	100	4.0–5.0	0.5	0.0	0.0	∞

Notes. [α] stands for the α elements enhancement with respect to solar (Caffau et al. 2011).

The specificity of the models in the range of $T_{\rm eff}$ suitable for GJ 758 B have not yet all been described in the literature. So it is important to make a description of the most relevant hypothesis in the models and differences between the models in this paper. The parameter space of the models is summarized in Table A.1.

The BT-Settl model couples a cloud model to a 1D radiative transfer code PHOENIX (Allard et al. 1994; Hauschildt et al. 1997). The model considers the formation of a cloud deck, which is composed of up to 55 grain species. The grain size and density, the abundances of chemicals in the gas phase, including the effect of element depletion induced by the grain formation, is computed layer per layer through the photosphere, following a comparison of the timescales for nucleation, condensation, gravitational settling or sedimentation, and mixing. Once rained out below the photosphere, the grain opacities are not accounted for in the radiative transfer. Nevertheless, these grains can still interact chemically with the gas phase. These models can predict the flux at the surface of a given object that is only defined by log g, $T_{\rm eff}$, and [Fe/H]. They account for the non-equilibrium chemistry of CO, CH_4, N_2, NH_3, and CO_2. The models predict the formation of a secondary (resurgent) cloud layer into the photosphere made up of Na_2S and MnS then of KCl, NaCl, and some ZnS that lies above the rained-out primary cloud layer that is located below the photosphere and that originally remains in the atmosphere of L and early-T dwarfs. Here we used the 2014 releases of the models (hereafter BT-SETTL14), which include revised alkali cloud opacities and the latest CIA opacities (Abel et al. 2012). A specific grid was computed for the project to cover the Y-dwarf temperature domain (hereafter BT-SETTL14-Y), in addition to the already existing grid that covers a broader interval of $T_{\rm eff}$ and that considers α-element enrichment (hereafter BT-SETTL14).

The 1D Exo-REM models (Baudino et al. 2015) propose a simplified approach of substellar atmospheres. They predict the equilibrium-temperature profile and mixing-ratio profiles of the most important gases (H2-He collision-induced absorption, H_2O, CO, CH_4, NH_3, VO, TiO, Na, and K). The absorption by iron and silicate cloud particles is added above the expected condensation levels with a fixed-scale height and a given optical depth at a given reference wavelength. For the purpose of the GJ 758 B study, two grids of models – NC and T3 – were computed. The NC models consider photospheres with no cloud opacity. The T3 models consider a photosphere with 30 μm Iron (Fe) and Forsterite (Mg_2SiO_4) grains and an optical depth of reference $\tau_{\rm cloud} = 3$. The grains are located between the condensation level and a 100 times lower pressure. They have scale heights equal to the gas-scale height, and optical depths of 3 and 0.45 at 1.2 μm, respectively, for Fe and Mg_2SiO_4.

Similarly to the BT-Settl models, the Morley+12 models account for the possible resurgence of clouds in late-T dwarf atmospheres. These 1D models build on the cloud model of Ackerman & Marley (2001). The cloud content (and opacity) is determined by a balance between the upward transport by turbulent mixing with the sedimentation. The Ackerman & Marley (2001) models do not compute the microphysics associated in the clouds, but instead leave as free parameters the vertical eddy diffusion coefficient K_{zz} and a sedimentation efficiency parameter $f_{\rm sed}$. A higher $f_{\rm sed}$ corresponds to thinner (rained-out) clouds. In the case of the Morley+12 models, non-equilibrium chemistry is not included, so that only models with $K_{zz} = 0$ are available and they only enable an exploration of the $f_{\rm sed}$. As a second difference to the BT-Settl, the Morley+12 models do not account for chemical reactions between the condensed species and the gas phase. Finally, we added the models of Saumon et al. (2012) to this grid, which are also based on Ackerman & Marley (2001) models, to explore the case of an extreme sedimentation efficiency (cloud-free atmospheres).